

State-space kinetic Ising model reveals task-dependent entropy flow in sparsely active nonequilibrium neuronal dynamics

Ken Ishihara^{1*,2}, Hideaki Shimazaki^{2,3*}

1 Graduate School of Life Sciences, Hokkaido University, Sapporo, Japan

2 Center for Human Nature, Artificial Intelligence, and Neuroscience (CHAIN), Hokkaido University, Sapporo, Japan

3 Department of Informatics, Kyoto University, Kyoto, Japan

* ishihara.ken.n7@elms.hokudai.ac.jp, h.shimazaki@i.kyoto-u.ac.jp

Abstract

Neuronal ensemble activity, including coordinated and oscillatory patterns, exhibits hallmarks of nonequilibrium systems with time-asymmetric trajectories to maintain their organization. However, assessing time asymmetry from neuronal spiking activity remains challenging. The kinetic Ising model provides a framework for studying the causal, nonequilibrium dynamics in spiking recurrent neural networks. Recent theoretical advances in this model have enabled time-asymmetry estimation from large-scale steady-state data. Yet, neuronal activity often exhibits time-varying firing rates and coupling strengths, violating steady-state assumption. To overcome these limitations, we developed a state-space kinetic Ising model that accounts for non-stationary and nonequilibrium properties of neural systems. This approach incorporates a mean-field method for estimating time-varying entropy flow, a key measure for maintaining the system's organization by dissipation. Applying this method to mouse visual cortex data revealed greater variability in causal couplings during task engagement despite the reduced neuronal activity with increased sparsity. Moreover, higher-performing mice exhibited increased entropy flow in higher-firing neurons during task engagement, suggesting that stronger directed activity emerged in a fewer neurons within sparsely active populations. These findings underscore the model's utility in uncovering intricate asymmetric causal dynamics in neuronal ensembles and linking them to behavior through the thermodynamic underpinnings of neural computation.

Introduction

The emergence of ordered spatiotemporal dynamics in nonequilibrium systems that continuously exchange energy and matter with their surroundings has intrigued many scientists [1–5], as it provides a foundational mechanism for phenomena such as chemical oscillations, morphogenesis, and collective behaviors like animal herding. Nonequilibrium processes inherently violate the detailed balance between the forward and reverse transitions, yielding time-asymmetric, irreversible dynamics. Stochastic thermodynamics has clarified that this time-asymmetry is essential for systems to sustain their organized structure by dissipating entropy into the environment [6–9].

Neural systems are no exception. In animals engaged in behavioral and cognitive tasks, the dynamics of neuronal population activity exhibit hallmarks of nonequilibrium systems. Notable examples include the rotational activity of M1 neurons during motor execution tasks [10, 11] and the sequential patterns observed in hippocampal neurons,

including their replay, during navigation and sleep [12–14]. Since the original proposal of cell assembly and its phase sequences by Donald O. Hebb [15], coordinated sequential patterns have been thought fundamental for memory consolidation and retrieval [16–19]. Recently, studies on fMRI or ECoG suggested that increased time-asymmetry in neural signals, quantified by steady-state entropy production [7, 20, 21], could serve as a signature of consciousness [22–25] or reflect cognitive load demanded by tasks [26]. For instance, entropy production measured from ECoG signals of non-human primates is diminished during sleep and certain types of anesthesia in comparison with wakefulness [22, 25], indicating that the awake state includes more directed temporal patterns. However, assessing entropy production directly from neuronal spiking activities remains challenging. Further complicating this issue, neural signals exhibit non-stationary dynamics, including oscillatory behavior, which hinders the use of steady-state entropy production metrics.

The kinetic Ising model is a prototypical model of recurrent neural networks [27, 28]. It extends the equilibrium Ising model, which has been successfully applied to empirical spiking data to elucidate the thermodynamic and associative-memory properties of neural systems [29, 30]. In the kinetic Ising system, neurons are causally driven by the past states of self and other neurons as well as a force representing intrinsic excitability of the neurons and/or an influence of unobserved concurrent signals. When neurons receive steady inputs and their causal couplings are asymmetric, the system does not relax to an equilibrium state. Instead, it exhibits steady-state nonequilibrium dynamics characterized by non-zero entropy production. Recent theoretical studies on steady-state entropy production have elucidated its behavior in relation to distinct phases of the Ising system, including critical phase transitions [31]. Mean-field theories have been developed for kinetic Ising systems [32–37], enabling the estimation of steady-state entropy production from large-scale spike sequences [37]. However, neuronal activity exhibits dynamical changes not only in firing rates but also in the strength of their interactions, both of which violate the steady-state assumptions.

To account for the non-stationary dynamics of neural systems, the state-space method [38, 39] has been applied to the Ising system [40–44]. In these approaches, Bayesian filtering and smoothing algorithms have been developed to estimate time-dependent parameters of the Ising model, along with an EM algorithm [45, 46] to optimize various hyper-parameters. These models have enabled researchers to trace time-varying neuronal interactions while neurons’ internal parameters change dynamically, absorbing the effect from unobserved concurrent signals. Additionally, it has elucidated the thermodynamic quantities of neural systems (e.g., free energy and specific heat) in a time-dependent manner, in relation to the behavioral paradigms of tasks [42]. Nevertheless, these methods assume an equilibrium Ising model with symmetric couplings, which limits their ability to assess the nonequilibrium properties of observed neural activities.

In this study, we develop the state-space kinetic Ising model to account for the non-stationary and nonequilibrium properties of neural activities and construct a mean-field method for estimating time-varying entropy flow, an essential component of entropy production that quantifies the dissipation of entropy, from spiking activities of neural ensembles. Application of the methods to mice V1 neurons revealed behavior-dependent changes in entropy flow. From the analysis of 37 mice, we found that while spike rates of the populations are lower on average and exhibited sparser distributions when mice actively engaged in tasks than in passive conditions, active engagement significantly enhanced the variability of the neuronal couplings, which contributed to increasing entropy flow. Further, in the mice with higher task performance, neurons with higher spike rates tended to increase entropy flow in active engagement. We corroborated these results by trial-shuffled data that excluded

influences of firing-rate dynamics and sampling errors in estimating neuronal couplings. These results suggest that, within the sparse population activity during active task engagement, stronger time-asymmetric causal activity appeared in a small fraction of neurons with higher spike rates in competent mice. Thus, the method enabled to reveal details of the behavior-related time-asymmetric causal activities in sparsely active neuronal populations.

This paper is organized as follows. In Results, we first introduce the state-space kinetic Ising model and its estimation method. Next, we introduce the mean-field method for estimating entropy flow. We validate these methods through simulations and then apply them to mice V1 data. Finally, we relate our findings with previous studies and discuss their implications in sparse population coding.

Results

The state-space kinetic Ising model

Model specifications

In neurophysiological experiments, the experimentalists simultaneously record the activity of multiple neurons while animals are exposed to a stimulus or perform a task and repeat the recordings multiple times under the same experimental conditions. We analyze the quasi-simultaneous activity of neurons using binarized spike sequences. For this goal, we convert the simultaneous sequences of spike timings of N neurons into sequences of binary patterns by binning them with a bin width of Δ [ms]. We assign a value of 1 if there is one or more spikes in a bin and 0 otherwise. We assume that there are $T + 1$ bins for each trial with an initial bin being 0-th bin, and L trials in total. Below we treat the bins as discrete time steps and refer to the t -th bin as time t . We let $x_{i,t}^l = \{0, 1\}$ be a binary variable at time t in the l -th trial ($i = 1, \dots, N$, $t = 0, \dots, T$, $l = 1, \dots, L$). We collectively denote the binary patterns of simultaneously recorded neurons at time t in the l -th trial using a vector, $\mathbf{x}_t^l = (x_{1,t}^l, \dots, x_{i,t}^l, \dots, x_{N,t}^l)$. Further, we denote the patterns at time step t from all trials by $\mathbf{x}_t = (\mathbf{x}_t^1, \dots, \mathbf{x}_t^L, \dots, \mathbf{x}_t^L)$ and denote all the patterns up to time t by $\mathbf{x}_{0:t}$.

We construct the state-space kinetic Ising model to account for the nonequilibrium dynamics of the binary sequences by extending the state-space models developed for equilibrium Ising systems [41, 42]. The state-space model is composed of the observation model and the state model. The observation model in the t -th bin is

$$\begin{aligned} p(\mathbf{x}_t | \mathbf{x}_{t-1}, \boldsymbol{\theta}_t) &= \prod_{l=1}^L \prod_{i=1}^N p(x_{i,t}^l | \mathbf{x}_{t-1}^l, \boldsymbol{\theta}_t^i) \\ &= \prod_{l=1}^L \prod_{i=1}^N \exp \left[\theta_{i,t} x_{i,t}^l + \sum_{j=1}^N \theta_{ij,t} x_{i,t}^l x_{j,t-1}^l - \psi(\boldsymbol{\theta}_t^i, \mathbf{x}_{t-1}^l) \right], \end{aligned} \quad (1)$$

where $\theta_{i,t}$ is a time-dependent (external) field parameter that determines the bias for inputs to the i -th neuron at time t and $\theta_{ij,t}$ is a time-dependent coupling parameter from the j -th neuron to the i -th neuron. These parameters are collectively denoted as $\boldsymbol{\theta}_t = (\boldsymbol{\theta}_t^1, \dots, \boldsymbol{\theta}_t^i, \dots, \boldsymbol{\theta}_t^N)$ and $\boldsymbol{\theta}_t^i = (\theta_{i,t}, \theta_{i1,t}, \dots, \theta_{ij,t}, \dots, \theta_{iN,t})$. Furthermore, $\psi(\boldsymbol{\theta}_t^i, \mathbf{x}_{t-1}^l)$ is the log normalization term defined as

$$\psi(\boldsymbol{\theta}_t^i, \mathbf{x}_{t-1}^l) = \log \left[1 + \exp \left[\theta_{i,t} + \sum_{j=1}^N \theta_{ij,t} x_{j,t-1}^l \right] \right]. \quad (2)$$

We also specify $p(\mathbf{x}_0)$, a probability mass function of the binary patterns at time $t = 0$, which we assume $p(\mathbf{x}_0) = \prod_{i=1}^N \prod_{l=1}^L p(x_{i,0}^l)$, where $p(x_{i,0}^l) = 0.5$.

Next, we introduce a state model of the time-varying parameters $\boldsymbol{\theta}_t$ for $t = 1, \dots, T$:

$$p(\boldsymbol{\theta}_{1:T}|\mathbf{w}) = \prod_{i=1}^N \left[p(\boldsymbol{\theta}_1^i | \boldsymbol{\mu}^i, \boldsymbol{\Sigma}^i) \prod_{t=2}^T p(\boldsymbol{\theta}_t^i | \boldsymbol{\theta}_{t-1}^i, \mathbf{Q}^i) \right], \quad (3)$$

where \mathbf{w} denotes the collection of the hyper-parameters:

$\mathbf{w} = [\boldsymbol{\mu}^1, \dots, \boldsymbol{\mu}^N, \boldsymbol{\Sigma}^1, \dots, \boldsymbol{\Sigma}^N, \mathbf{Q}^1, \dots, \mathbf{Q}^N]$. Namely, we assume independence of the parameters of a neuron from those of the other neurons, which significantly reduces computational costs. The transition of the i -th neurons follows the linear Gaussian models:

$$p(\boldsymbol{\theta}_t^i | \boldsymbol{\theta}_{t-1}^i, \mathbf{Q}^i) = \frac{1}{\sqrt{|2\pi\mathbf{Q}^i|}} \exp \left[\frac{1}{2} (\boldsymbol{\theta}_t^i - \boldsymbol{\theta}_{t-1}^i)^\top (\mathbf{Q}^i)^{-1} (\boldsymbol{\theta}_t^i - \boldsymbol{\theta}_{t-1}^i) \right], \quad (4)$$

while the initial density is given by $p(\boldsymbol{\theta}_1^i | \boldsymbol{\mu}^i, \boldsymbol{\Sigma}^i) = \mathcal{N}(\boldsymbol{\mu}^i, \boldsymbol{\Sigma}^i)$.

Estimating the time-dependent parameters using optimized hyper-parameters

Our goal is to obtain the approximation of the posterior density of the trajectory $\boldsymbol{\theta}_{1:T}$ given the observed neural activity $\mathbf{x}_{0:T}$:

$$p(\boldsymbol{\theta}_{1:T} | \mathbf{x}_{0:T}, \mathbf{w}) = \frac{p(\mathbf{x}_{0:T} | \boldsymbol{\theta}_{1:T}) p(\boldsymbol{\theta}_{1:T} | \mathbf{w})}{p(\mathbf{x}_{0:T} | \mathbf{w})}, \quad (5)$$

while optimizing the parameter \mathbf{w} under the principle of maximizing marginal likelihood:

$$\begin{aligned} p(\mathbf{x}_{0:T} | \mathbf{w}) &= p(\mathbf{x}_0) \prod_{t=1}^T p(\mathbf{x}_t | \mathbf{x}_{0:t-1}, \mathbf{w}) \\ &= p(\mathbf{x}_0) \prod_{t=1}^T \prod_{l=1}^L \prod_{i=1}^N \int p(x_{i,t}^l | \mathbf{x}_{t-1}^l, \boldsymbol{\theta}_t^i) p(\boldsymbol{\theta}_t^i | \mathbf{x}_{0:t-1}^l, \mathbf{w}) d\boldsymbol{\theta}_t^i. \end{aligned} \quad (6)$$

Here, $p(\boldsymbol{\theta}_t^i | \mathbf{x}_{0:t-1}^l, \mathbf{w})$ is the one-step prediction density.

The Expectation-Maximization (EM) algorithm [47] offers a way to construct the approximate posterior with optimized hyperparameters by alternately constructing the approximate posterior density while fixing the parameters (E-step) and optimizing the parameters while fixing the approximate posterior (M-step). The construction of the approximate posterior density at the E-step is performed by sequentially applying Bayes algorithms in a forward and backward manner, where we approximate the posteriors by Gaussian distributions using the Laplace's method. Thus, the method yields the mean and variance of the approximated Gaussian posterior at time t , which are denoted as $\boldsymbol{\theta}_{t|T}$ and $\mathbf{W}_{t|T}$, respectively. See Methods for the details of the algorithm.

Estimating entropy flow

Using the learned parameters $\boldsymbol{\theta}_{1:T}$ of the kinetic Ising model from spike data, we estimate entropy flow (also known as bath entropy change) at each time step. The entropy flow at time t is defined as:

$$\sigma_t^{\text{flow}} = \sum_{\mathbf{x}_t, \mathbf{x}_{t-1}} p(\mathbf{x}_t, \mathbf{x}_{t-1}) \log \frac{p(\mathbf{x}_t | \mathbf{x}_{t-1})}{p(\mathbf{x}_{t-1} | \mathbf{x}_t)}, \quad (7)$$

where $p(\mathbf{x}_{t-1} | \mathbf{x}_t)$ represents the probability of observing time-reversed processes generated under the forward model. Eq. 7 is related to the entropy production σ_t at time t [7, 9, 20, 21] as follows:

$$\begin{aligned}\sigma_t &= \sum_{\mathbf{x}_t, \mathbf{x}_{t-1}} p(\mathbf{x}_t, \mathbf{x}_{t-1}) \log \frac{p(\mathbf{x}_t | \mathbf{x}_{t-1}) p_{t-1}(\mathbf{x}_{t-1})}{p(\mathbf{x}_{t-1} | \mathbf{x}_t) p_t(\mathbf{x}_t)} \\ &= (S_t - S_{t-1}) + \sigma_t^{\text{flow}}.\end{aligned}\quad (8)$$

Here $p_t(\mathbf{x}_t)$ is the marginal probability mass function of the system at time t . S_t is the entropy of the system at time t defined as

$$S_t = - \sum_{\mathbf{x}_t} p_t(\mathbf{x}_t) \log p_t(\mathbf{x}_t).\quad (9)$$

The entropy production is non-negative: $\sigma_t \geq 0$. Thus, the positive entropy flow allows a decrease in the system's entropy: namely the system can be more structured or organized when the entropy flow is positive. Since it is challenging to estimate the system's entropy or its change, here we estimate the entropy flow, which provides the lower bound of the entropy change: $S_t - S_{t-1} \geq -\sigma_t^{\text{flow}}$. Similarly, since the total entropy production across all time steps $\sigma_{1:T}$ is given as

$$\sigma_{1:T} = \sum_{t=1}^T \sigma_t = (S_T - S_0) + \sum_{t=1}^T \sigma_t^{\text{flow}},\quad (10)$$

the total entropy flow $\sum_{t=1}^T \sigma_t^{\text{flow}}$ provides the lower bound of the system's entropy change from the initial and final time step: $S_T - S_0 \geq -\sum_{t=1}^T \sigma_t^{\text{flow}}$. This indicates that the positive total entropy flow enables the systems to be more structured at the final time step than at the initial time step.

In this study, we refer to Eq. 7 as 'entropy flow' because it is related to heat flow to reservoirs (thermal bath) and the entropy change of the reservoirs in thermodynamics [48]. We note that Eq. 7 differs from the entropy flow defined in [49, 50], which was obtained by the decomposition of the dissipation function [21] as an alternative of entropy production. See [21, 51] for their distinct definitions and decompositions for the case of discrete-time systems.

For the case of the kinetic Ising model, the entropy flow is written as

$$\begin{aligned}\sigma_t^{\text{flow}} &= \sum_i \theta_{i,t} (E_{\mathbf{x}_t} x_{i,t} - E_{\mathbf{x}_{t-1}} x_{i,t-1}) + \sum_{i,j} \theta_{ij,t} E_{\mathbf{x}_t, \mathbf{x}_{t-1}} (x_{i,t} x_{j,t-1} - x_{i,t-1} x_{j,t}) \\ &\quad - \sum_i (E_{\mathbf{x}_{t-1}} \psi(\theta_t^i, \mathbf{x}_{t-1}) - E_{\mathbf{x}_t} \psi(\theta_{t-1}^i, \mathbf{x}_t))\end{aligned}\quad (11)$$

where $E_{\mathbf{x}_t}$ and $E_{\mathbf{x}_t, \mathbf{x}_{t-1}}$ represents expectation by $p(\mathbf{x}_t)$ and $p(\mathbf{x}_t, \mathbf{x}_{t-1})$, respectively. In the steady state with time-independent parameters, only the second term remains, which can be quantified by the couplings and delayed correlations [37]. Conversely, when the couplings are zero, the entropy flow is determined by the first and third terms, which depend only on the marginal probability $p(\mathbf{x}_t)$.

Mean-field method for estimating entropy flow

Entropy flow (Eq. 7) requires the expectation by the joint density $p(\mathbf{x}_t, \mathbf{x}_{t-1})$, which is time-consuming for large systems. While the mean-field methods for the kinetic Ising model [32–37] were employed to estimate steady-state entropy flow [37], the mean-field

method for estimating time-varying entropy flow remains unexplored. Here we develop the mean-field method for estimating dynamic entropy flow.

The entropy flow σ_t^{flow} can be decomposed into the forward and reversed components,

$$\sigma_t^{\text{flow}} = -\sigma_t^{\text{forward}} + \sigma_t^{\text{backward}}, \quad (12)$$

where $\sigma_t^{\text{forward}}$ and $\sigma_t^{\text{backward}}$ are the entropy of the conditional and time-reversed conditional distribution, respectively. The proposed mean-field method estimates the entropy flow by approximating the forward and time-reversed conditional entropy using the Gaussian integral:

$$\sigma_t^{\text{forward}} \approx \sum_{i=1}^N \int \mathcal{D}_z \chi(g_{i,t} + z\sqrt{\Delta_{i,t}}), \quad (13)$$

$$\sigma_t^{\text{backward}} \approx \sum_{i=1}^N \int \mathcal{D}_z \phi_i(g_{i,t} + z\sqrt{\Delta_{i,t}}), \quad (14)$$

where $\mathcal{D}_z = \frac{dz}{\sqrt{2\pi}} \exp(-\frac{1}{2}z^2)$. See Methods for derivation of these results. The functions $\chi(h)$ and $\phi_i(h)$ are given as follows. $\chi(h)$ is entropy of (0, 1) binary random variables with mean $r(h) = 1/(1 + e^{-h})$:

$$\chi(h) = -r(h) \log r(h) - (1 - r(h)) \log(1 - r(h)). \quad (15)$$

$\phi_i(h)$ is given by

$$\phi_i(h) = -(m_{i,t-1}h - \psi(h)), \quad (16)$$

where $m_{i,t-1}$ is the mean-field activation rate of i -th neuron at time $t - 1$ (see below for how to obtain it).

Here the input h is a Gaussian random variable with mean $g_{i,t}$ and variance $\Delta_{i,t}$, which can be computed as $h = g_{i,t} + z\sqrt{\Delta_{i,t}}$ using a standardized Gaussian random variable z . $g_{i,t}$ and $\Delta_{i,t}$ are computed using the mean-field activation rate at the previous step $m_{i,t-1}$ as

$$g_{i,t} = \theta_{i,t} + \sum_j \theta_{ij,t} m_{j,t-1}, \quad (17)$$

$$\Delta_{i,t} = \sum_j \theta_{ij,t}^2 m_{j,t-1} (1 - m_{j,t-1}). \quad (18)$$

The mean-field activation rate $m_{i,t}$ ($i = 1, \dots, N, t = 1, \dots, T$) can be recursively computed using

$$m_{i,t} \approx \int \mathcal{D}_x r(g_{i,t} + x\sqrt{\Delta_{i,t}}), \quad (19)$$

starting with nominal values of $m_{i,0}$. In this study, we use spiking probability averaged over all time bins and trials for each neuron as $m_{i,0}$.

Application to simulated data

Estimating the model parameters from simulated data

We start testing the proposed method by estimating the time-dependent parameters of a kinetic Ising model consisting of two simulated neurons (Fig. 1A). Figure 1B shows

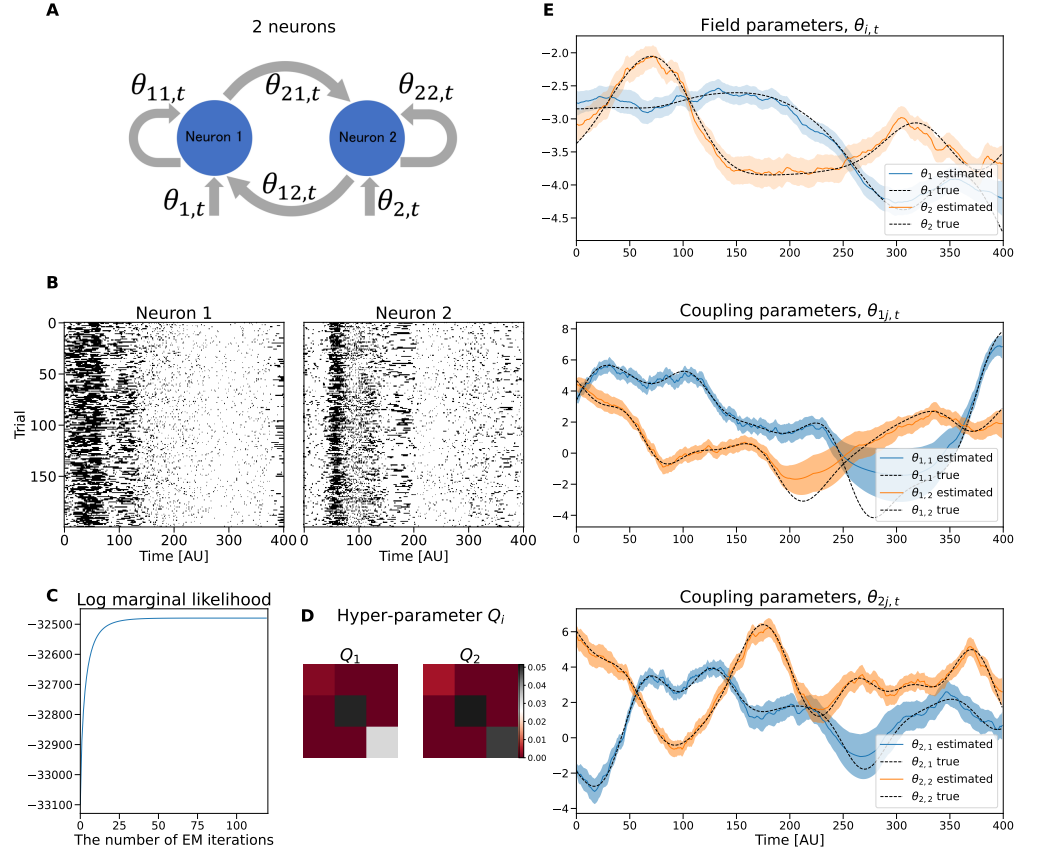


Fig 1. Application of the state-space kinetic Ising model to two simulated neurons. **A** A schematic of the time-dependent kinetic Ising model for two neurons with field and coupling parameters. The links between the nodes represent the neurons' causal interactions with arrows indicating the time evolution from the past to the present. **B** Raster plots for the two neurons. The vertical axis represents the number of trials, and the horizontal axis shows the number of time bins. **C** The approximate marginal log-likelihood as a function of the iteration steps of the EM algorithm. **D** The optimized hyperparameter \mathbf{Q}^i for neuron 1 (left) and neuron 2 (right). **E** (top) Estimated and true time-dependent field parameters. The solid lines represent the MAP estimates of the first-order parameters obtained from the smoothing posterior $\theta_{t|T}$. The shaded areas show the 95% credible intervals derived from the diagonal elements of the smoothed covariance matrix. The dotted lines are the true θ_t^i used to generate the data. (middle, bottom) Estimated and true time-dependent coupling parameters. The solid lines represent the MAP estimates of the second-order parameters.

the spike data generated using Eq. (1) with the number of bins, $T = 400$, and the number of trials, $R = 200$. The time-dependent parameter θ_t used in the data generation process was sampled from Gaussian processes.

The EM algorithm, as described in Methods, was applied to this spike data until the log marginal likelihood converges (Fig. 1C). Figure 1D shows the components of the optimized hyperparameter matrices, \mathbf{Q}^i ($i = 1, 2$). Figures 1E show the MAP estimates of the time-dependent fields $\theta_{i,t}$ and interactions $\theta_{ij,t}$ under the optimized hyperparameters (solid lines) with 95% credible intervals (shaded areas). The results confirm that the method uncovers the underlying time-dependent parameters (black

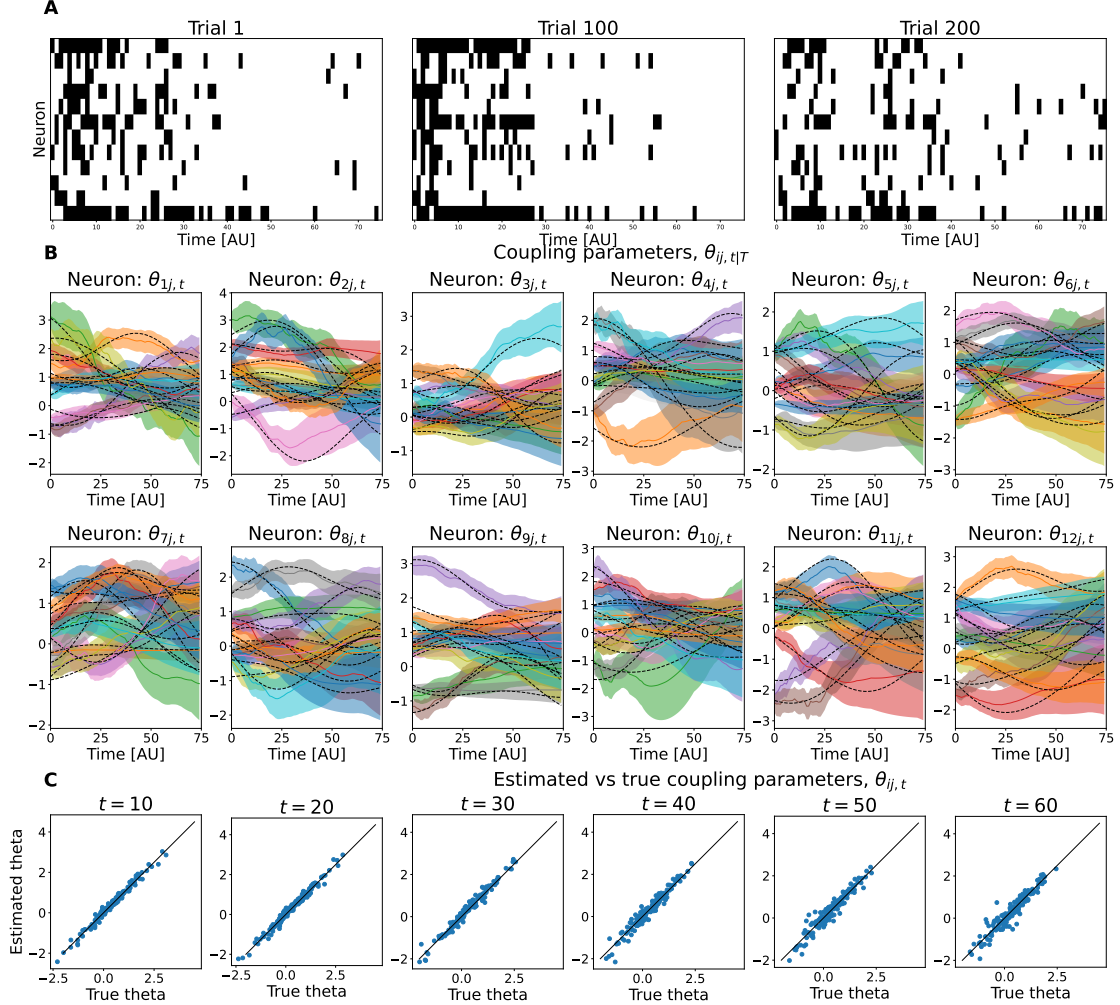


Fig 2. The application of the state-space kinetic Ising model to 12 simulated neurons. A Simulated spike data for the first, 100th, and last trial out of 200 trials. The vertical axis shows the number of neurons, and the horizontal axis represents the number of bins. **B** Estimated coupling parameters $\theta_{t|T}$, for all neurons and time bins ($i = 1, 2, \dots, 12, t = 1, \dots, T$). **C** Scatter plots comparing the true coupling parameters θ_t with the estimated values $\theta_{t|T}$ at time $t = 10, 20, \dots, 60$. The black line is a diagonal line.

dashed lines) used to generate the data.

Next, we applied the state-space kinetic Ising model to a network of 12 simulated neurons to estimate the time-varying field and coupling parameters between neurons. Figure 2A presents the spike data generated using the observation model with the number of bins set to $T = 75$ and the number of trials $R = 200$. Data simulation and estimation procedures follow the two-neuron case above. Figure 2B shows the estimated time-varying coupling parameters $\theta_{ij,t}$ for each neuron. These plots show only the couplings that are significantly deviated from zero: The couplings whose 95% credible interval contain 0 in all bins were excluded. In Fig. 2C, we compare the estimated coupling parameters $\theta_{t|T}$ with the true values θ_t at representative time points ($t = 10, 20, \dots, 60$). The scatter plot shows agreement between the true and estimated values, with most points aligning closely along the diagonal line, indicating that the

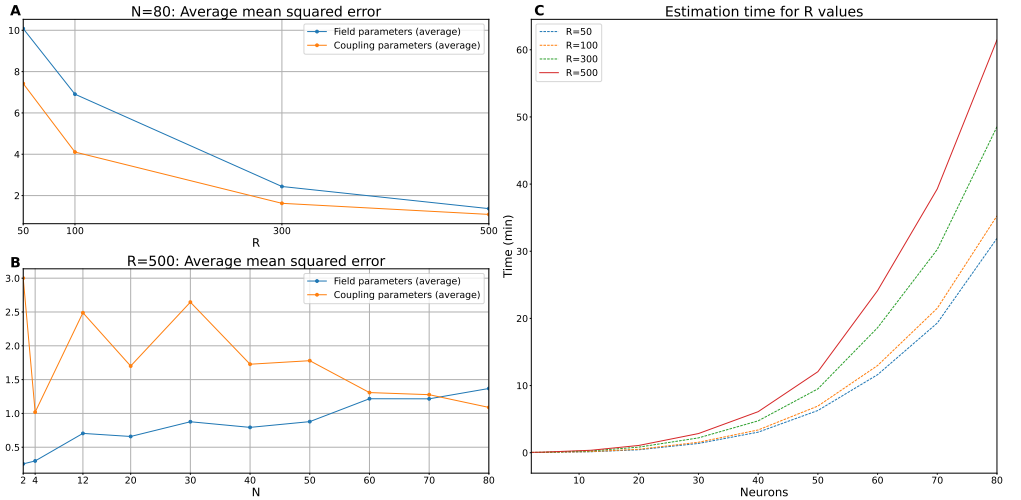


Fig 3. Estimation error and computational time. **A** Mean-squared error (MSE) for field and coupling parameters as a function of trials R with neurons fixed at $N = 80$. The number of EM iterations is fixed at 120. **B** Average MSE for field and coupling parameters as a function of neurons N with trials fixed at $R = 600$. **C** Estimation time as a function of neurons N for $R = 50, 100, 300, 500$. The computation was performed on Dell PowerEdge server with 2 CPUs of Intel Xeon 2.4G.

model captured the underlying dynamics of the coupling parameters. These results confirm that the proposed state-space kinetic Ising model can reliably estimate time-varying coupling parameters in a network of simulated neurons.

Estimation error and computational time

We evaluate the performance of the proposed state-space kinetic Ising model in terms of both estimation accuracy and computational time, while varying the size of the dataset and population.

Estimation error We calculated a mean-squared error (MSE) to evaluate the degree of agreement between the true parameter values $\theta_{1:T}$ and the estimated values $\theta_{1:t|T}$ for the field and coupling parameters. More specifically, the MSEs of the field $\theta_{i,t}$ and coupling $\theta_{ij,t}$ parameters were averaged over time bins, which were then averaged over the set of parameters to yield scalar results. Figures 3A, B present the results for cases where $N = 80$ and $R = 550$ are fixed, respectively. Here, regardless of the (R, N) combination, the number of EM iterations was set to 120.

When the number of neurons was fixed at $N = 80$, the MSEs for both the field and coupling parameters decreased as the number of trials R increased (Fig. 3A), indicating that estimation accuracy improves with an increasing amount of trials. Conversely, when the number of trials R was fixed at 600 and the number of neurons N increased, the average MSE for the fields increased (Fig. 3B). The average MSE for the couplings did not increase in this simulation, within the range of the neuron number analyzed.

Computational time We analyzed the computation time for model fitting. Our assumption of independent state evolution for individual neurons (Eq. 3) significantly reduces computational costs. This enables separate calculations for filtering, smoothing, and parameter optimization per neuron, which can be further accelerated through parallel updates. However, heterogeneous couplings assumed in the model increase computational complexity. Figure 3C shows the relationship between the computational time to complete the EM algorithm under the different number of neurons N and trials

R . The results indicate that estimating population dynamics with $N = 80$ using $R = 500$ trials can be completed by approximately an hour, which is feasible for practical data analyses. Nevertheless, computation time is scaled with N and R . The result suggests that reducing computation time through further optimization is necessary for enabling larger-scale analysis. For instance, the current filtering method performs exact calculations to find MAP estimates of the posterior using the Newton-Raphson method, which can be accelerated by using quasi-Newton or mean-field methods, as demonstrated in the equilibrium state-space Ising model [42].

Estimating entropy flow of simulation data

In this section, we assess the proposed mean-field approximation method for estimating entropy flow. As in the previous section, we generated spike samples from time-dependent parameters θ_t sampled from Gaussian processes. All simulations were conducted with $N = 80$, $T = 75$, and $R = 550$ trials. We then estimated the time-dependent field and coupling parameters from the data. Using the posterior mean $\theta_{t|T}$, we obtained the mean-field approximation of the time-dependent entropy flow (Eqs. 13 and 14). The red line in Fig. 4 represents the entropy flow calculated using the mean-field approximation with the learned parameters.

To verify the consistency of the estimated entropy flow, we calculated the entropy flow using a sampling-based method to compute the expectation over the two-step trajectories (blue line). This approach involves repeatedly running the kinetic Ising model (Eq. 1) using the true parameters to sample spike time series data. This process was performed $n_s = 10,000$ times to empirically estimate the joint distribution $p(\mathbf{x}_t, \mathbf{x}_{t-1})$. Using this empirical distribution, we obtained a sample estimate of the entropy flow as follows

$$\hat{\sigma}_t^{\text{flow}} = \frac{1}{n_s} \sum_{s=1}^{n_s} \log \frac{p(\mathbf{x}_t^s | \mathbf{x}_{t-1}^s)}{p(\mathbf{x}_{t-1}^s | \mathbf{x}_t^s)}. \quad (20)$$

This sampling estimation using the true parameters serves as the baseline.

The mean-field estimation of the entropy flow (red) follows the trajectory of the baseline sampling estimation using the true parameters (blue). The result confirms the proposed method is applicable for entropy flow analysis while ensuring computational

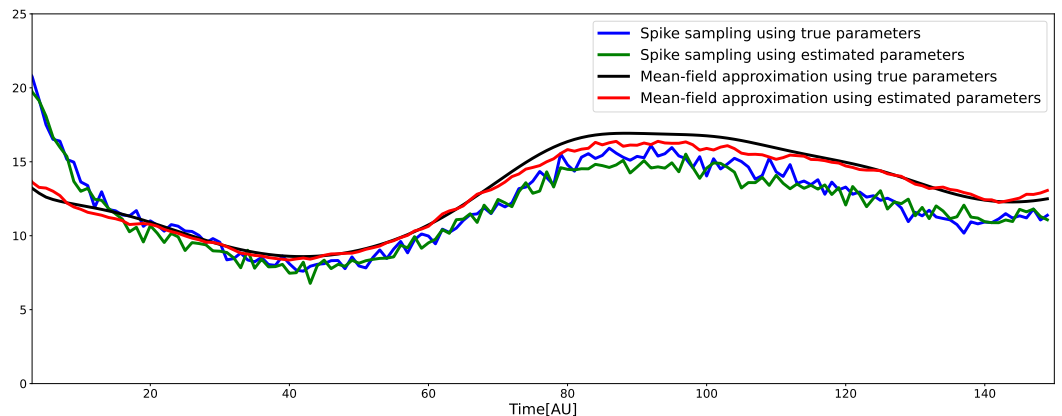


Fig 4. Comparison of entropy flow estimation methods. Entropy flows estimated by four different methods: Sampling method using true parameters θ_t (blue); Sampling method using estimated parameters $\theta_{t|T}$ (green); Mean-field method using true parameters θ_t (black); Mean-field method using estimated parameters $\theta_{t|T}$ (red).

feasibility. The slight discrepancy between the two lines is due to the errors in estimating the time-dependent parameters and/or the mean-field approximation (in addition to sampling fluctuation inherent to the sampling method). To separate these effects, we estimated the entropy flow by the mean-field approximation using the true parameters θ_t used for the data generation (black). This estimation was deviated from the baseline sampling estimation. In contrast, the sampling method using estimated parameters (green) did not significantly differ from the baseline. Thus, the mean-field approximation introduced errors rather than inaccuracies in parameter estimation. These results indicate that further enhancement of the estimation accuracy is possible by refining the mean-field method.

Application to mouse V1 neurons under active and passive exposures to visual stimuli

Having confirmed the applicability of our methods using simulation data, we next applied the state-space kinetic Ising model to empirical data obtained from mice exposed to visual stimuli and estimated its entropy flow.

Experimental design and data description

In this study, we analyzed the “Allen Brain Observatory: Visual Behavior Neuropixels” dataset provided by the Allen Institute for Brain Science, which contains large-scale recordings of neural spiking activity of mouse brains during the visual change detection task (See [52–54] for the analyses using this data set). The task is designed to analyze the effect of novelty and familiarity of the stimulus on neural responses. One of two image sets (G and H) were presented to animals at the training/habituation and recording sessions with different orders. The G and H image sets contain 8 natural images. We analyzed the recordings of 37 mice available from the Allen dataset, which were exposed to stimulus G in the recording sessions (either day 1 or 2) whereas the same stimulus G was used in the training and habituation sessions prior to the recording sessions (i.e., the case in which G is familiar).

The neural activities were recorded under two distinct conditions, in which the mice were either actively or passively performing the task under the same set of images. The active condition involved the mice performing a go/no-go change detection task, where they earned a water reward upon detection of a change in the visual stimulus, measured by licking behavior. Each of the 8 stimuli was presented for 250 ms, followed by a 500 ms interstimulus interval (gray screen), repeating for one hour while mice actively engaged in the task for reward. In contrast, the passive condition involved replaying the same visual stimuli used in the active condition but without providing any rewards or access to the lick port. In this study, we focused on analyzing recordings with a single image labeled im036.r, which is used in the training session and classified as ‘Familiar,’ and compared neural responses under the active and passive conditions. We used all presentations of the images equally and treated one presentation as a trial.

We selected neurons in the V1 area for analysis. For each mouse, we analyzed simultaneous activities of neurons with length 750 ms after the onset of the image im036.r, which resulted in R trials. While the number of trials varies across mice, the mean trial number was $R = 566$ with 356 and 652 as the minimum and maximum number of trials.

Estimating time-dependent parameters of the kinetic Ising for mice V1 data

We constructed binary sequences using a 10 ms bin, which results in $T = 75$ time bins. Figure 5A Left shows the probability of a spiking event within a bin averaged over

neurons at each time under the active and passive conditions (population-average spike rate) from an exemplary mouse (574078). The overall temporal profiles were similar across the active and passive conditions. In both conditions, the population exhibited higher mean spike rates during the stimulus presentation period (0-250 ms) than the post-stimulus period (250-750 ms). However, their magnitudes differed significantly. The passive condition (blue) showed consistently higher spiking probabilities than the active condition (red) throughout the stimulus and post-stimulus periods. In agreement with the population-average spike-rate dynamics, time-averaged spike rates of individual neurons exhibited a sparser distribution during the active condition compared to the passive condition (Fig. 5A Right). These results were consistently observed across all mice with a few exceptions (S1 Fig and S2 Fig). We compared the average mean activity and sparsity of the distributions under the two conditions for all 37 mice (S3 Fig). Sparsity of a non-negative firing rate distribution was quantified by the coefficient of variation (CV) [55]. The V1 neurons exhibited diminished, sparser firing rate distributions in the active condition than in the passive condition, as confirmed by the reduced mean spike rates ($p = 1.556 \times 10^{-8}$, Wilcoxon signed-rank test) and increased CVs ($p = 8.35 \times 10^{-8}$, Wilcoxon signed-rank test).

We then applied the state-space kinetic Ising model to the binary activities of these neurons. For this goal, we selected the top $N = 80$ neurons with the highest spike rates. The estimated dynamics of the field and coupling parameters exhibited variations in both active and passive conditions (Fig. 5B). Notably, the field parameters $\theta_{i,t}$ (the first column) follow the dynamics of the mean spike rate of the population with significant fluctuations. On the contrary, the dynamics of the coupling parameters $\theta_{ij,t}$ exhibited smoother transitions. To clarify the dynamics of the couplings, we show them in the matrix form at specific time points, $t = 5, 25, 35, 50$ (Fig. 5C; timing marked in black lines in Fig. 5A left). The neurons are indexed in the descending order of the average firing rates (Neuron 1 shows the highest firing rate). The top and bottom rows show the results of the active and passive conditions, respectively. Coupling strength is indicated by color, with red and blue representing positive and negative values, respectively. The results show that (i) the couplings exhibit significant variations with positive and negative values; (ii) the variations are stronger in the active condition than in the passive condition; (iii) the diagonal components of the couplings (self-correlations) mostly display negative correlations.

To corroborate the above observations, we performed the same analysis on the trial-shuffled data (S4 Fig). Trial-shuffled data reveal bias and variance in estimation under the assumption of neuronal independence. The result shows a significant reduction in the magnitude and variability of the couplings whereas self-couplings remained unchanged (note that the self-coupling remains after trial-shuffling). However, non-zero couplings persisted with stronger variations in the active condition than in the passive condition, reflecting sampling fluctuations due to the lower firing rates in the active condition. These findings indicate that the parameters observed in Fig. 5B,C include estimation noise, necessitating statistical analyses to confirm their significance.

We assessed key features in estimated models for all mice by comparing them with trial-shuffled data. Figure 6A-C illustrates these features using an exemplary mouse (5571078). Figure 6A, B shows distributions of time-averaged fields $\theta_{i,t}$ and couplings $\theta_{ij,t}$ under the active and passive conditions, while Figure 6C shows a scatter plot of time-averaged reciprocal couplings $\theta_{ij,t}$ vs $\theta_{ji,t}$ to evaluate coupling asymmetry. In the active condition, the medians of field parameters decreased, reflecting reduced firing rates, while the medians of couplings remained near zero in both conditions. Field and coupling parameter variances increased, and coupling asymmetry strengthened in the active condition. These trends were consistent across all mice (Fig. 6D-F). These features are key aspects of neural dynamics that are closely related to entropy flow.

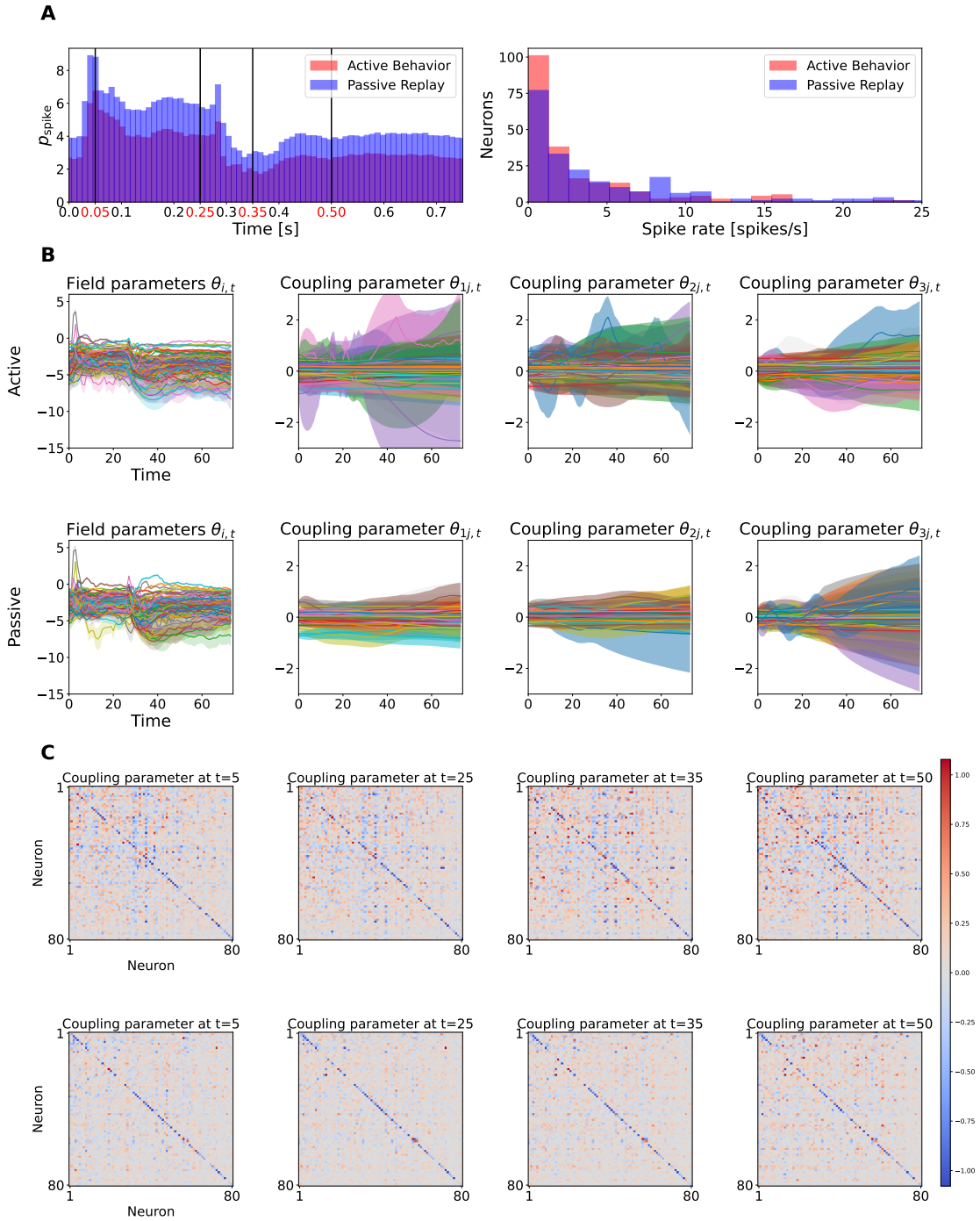


Fig 5. Estimated neural dynamics under the active and passive conditions for mouse 574078. **A** Spike-rate dynamics and distributions. (Left) Spiking probabilities averaged across neurons and trials with vertical lines marking time points analyzed in panel C. (Right) Spike-rate distributions of all recorded neurons. **B** Estimated time-dependent parameters $\theta_{t|T}$ of the kinetic Ising model under active (top) and passive (bottom) conditions. Each row shows estimates of the field $\theta_{i,t}$ and three representative coupling $\theta_{ij,t}$ parameters ($i = 1, 2, 3$). Solid lines and shaded areas indicate MAP estimates and 95% credible intervals. **C** Estimated couplings at $t = 5, 25, 35, 50$ under the active (top) and passive (bottom) conditions. Neurons are indexed in descending order of their average spike rates.

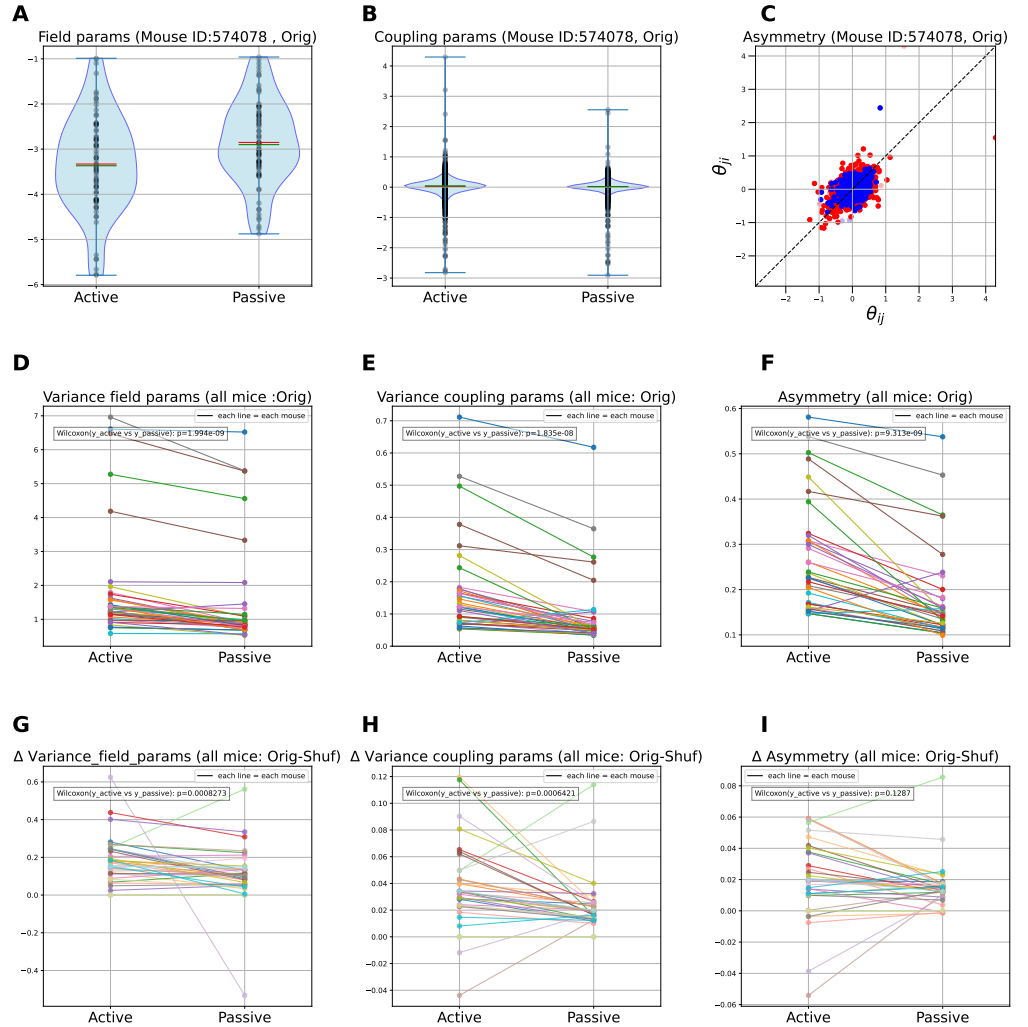


Fig 6. Variability of estimated model parameters. **A, B** Distributions of estimated field and coupling parameters under the active and passive conditions for mouse 574078. **C**: Scatter plots of coupling strength of reciprocal pairs under the active (red) and passive (blue) conditions for mouse 574078. The coupling asymmetries were 0.147 (active) and 0.105 (passive). The asymmetry was assessed by the average absolute difference of the reciprocal couplings $\langle |\bar{\theta}_{ij} - \bar{\theta}_{ji}| \rangle_{ij}$, where $\bar{\theta}_{ij}$ indicates time-average of $\theta_{ij,t}$ and $\langle \cdot \rangle_{ij}$ refers to the average over the combinations of i, j . **D-F** Group-level (all mice) comparisons for the original dataset: field variance (D), coupling variance (E), and coupling asymmetry (F). **G-I**: Plots analogous to D-F for shuffle-subtracted parameter variances and coupling asymmetry. Each subplot of D-I contains the p-values of Wilcoxon signed-rank tests for the active vs. passive conditions.

However, we also note that they are not entirely independent variables of each other, nor solely responsible for determining entropy flow.

While increased parameter variabilities and coupling asymmetry were observed under the active condition, they may be influenced by the lower neuronal activity. To examine this, we compared results with trial-shuffled data across all mice. Figures 6G-I show field and coupling variances and coupling asymmetry in both conditions, adjusted by subtracting shuffled data values for each mouse. Notably, observed values in both active and passive conditions were significantly higher than shuffled data ($p = 2.91 \times 10^{-11}$ (active), $p = 1.103 \times 10^{-7}$ (passive) for fields, $p = 4.676 \times 10^{-8}$ (active), $p = 1.455 \times 10^{-11}$ (passive) for couplings, and $p = 1.185 \times 10^{-5}$ (active), $p = 0.1287$ (passive) for asymmetry, Wilcoxon signed-rank test). Note that the observed significant heterogeneity in the field parameters is likely associated with the coupling heterogeneity. These results confirm that the variability and asymmetry observed in active or passive conditions are not explained by noise couplings.

Comparisons of these significant changes of the parameter variability (i.e., shuffled results subtracted) between the active and passive conditions showed significantly greater values in the active condition ($p = 8.273 \times 10^{-4}$ for fields, $p = 6.421 \times 10^{-4}$ for couplings, Wilcoxon signed-rank test, Fig.6G,H), indicating greater variabilities in both field and coupling parameters during active behavior. In contrast, coupling asymmetry showed no significant difference ($p = 0.1287$, Wilcoxon signed-rank test, Fig.6I). These findings validate enhanced parameter variability in the sparse neuronal activity during active engagement.

Entropy flow dynamics

Using the estimated parameters of the state-space kinetic Ising model, we computed entropy flow dynamics. Figure 7A shows the time-varying entropy flow of a representative mouse (574078) under the active and passive conditions (red and blue solid lines, respectively). In both cases, transient increases in entropy flow coincided with declines in the mean population spike rate (dashed lines). Similar patterns appeared across all mice analyzed (S5 Fig). These increases align with the second law, indicating that greater entropy dissipation is required when the system is transitioning to a lower entropy state, characterized by reduced firing rates.

The entropy flow time courses for this mouse showed no clear differences between the active and passive conditions. To assess population-level effects, we analyzed all 37 mice and computed total entropy flow across time bins for each condition (Fig. 7B). The comparison revealed significantly lower total entropy flow in the active condition ($p = 0.01159$, Wilcoxon signed-rank test). Note that neurons exhibited reduced firing rates (Fig. S3 Fig) and increased parameter variability (Fig. 6D,E) during the active condition. According to theoretical analyses of the kinetic fully-asymmetric Sherrington-Kirkpatrick (SK) model [31], increased coupling variability predicts higher entropy flow (Fig. 3c in [31]). In contrast, increased variability in the field parameters results in reduced entropy flow in the disordered (paramagnetic) phase (Fig. 6c in [31]). Thus, the expected increase of entropy flow by the increased coupling variabilities may be offset by reduced field magnitude and increased variability in the active condition.

To isolate the effect of couplings, we compared the observed total entropy flows with shuffled data results (Fig.7C). The estimated entropy flow for shuffled data includes the impact of firing rate dynamics and estimation error on couplings from other neurons; therefore, subtracting shuffling results from observed entropy flow isolates contributions of couplings among different neurons beyond the sampling fluctuation. Positive values of the shuffle-subtracted total entropy flow in both conditions indicate that the couplings caused a significant entropy flow increase ($p = 1.455 \times 10^{-11}$ for active, $p = 1.455 \times 10^{-11}$ for passive, Wilcoxon signed-rank test). These shuffle-subtracted

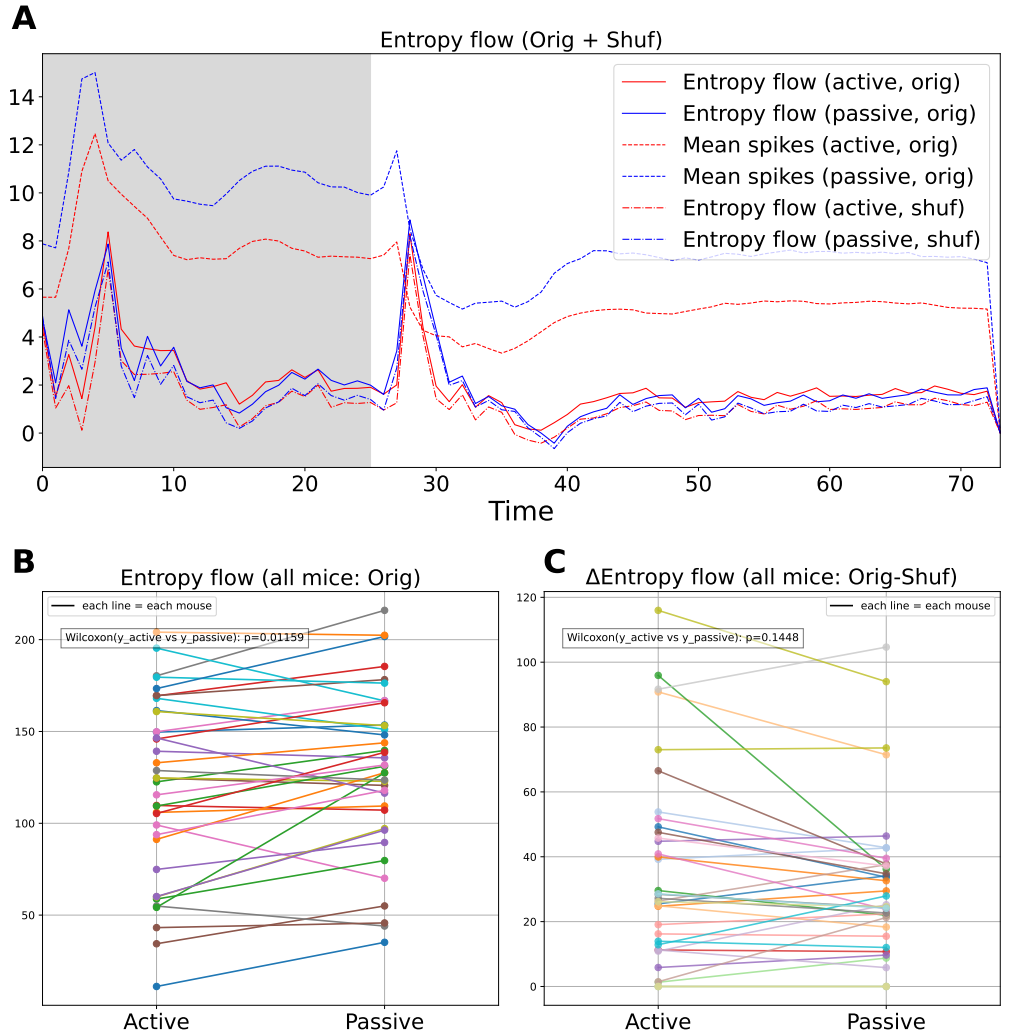


Fig 7. A Time courses of dissipative entropy for the original (solid) and shuffled data (dash-dot) under the active and passive conditions. The plot also shows time courses of the averaged population spike rates (dashed). The same color is used for the lines under the same condition. **B** Total entropy flows summed across all time bins for each mouse under the active and passive conditions. The same mouse is connected by a line. **C** Shuffled-subtracted total entropy flow (original - shuffle), plotted per mouse under the active and passive conditions.

entropy flows behave in agreement with the theoretical prediction by the SK model. In the active condition, the increased coupling variability (and asymmetry) from the shuffle-subtracted values were positively correlated with the shuffle-subtracted entropy flows, while the increased field heterogeneity was negatively correlated (S6 Fig.A-C). These effects disappeared in the passive condition, possibly due to small changes in the variabilities and asymmetry introduced by shuffling (S6 Fig.D-F).

Finally, we analyzed the differences in coupling-related entropy flows between the active and passive conditions for all mice (Fig.7C). The result shows no significant difference between the two conditions ($p = 0.1448$, Wilcoxon signed-rank test). However, these coupling-related entropy flows having the same magnitude emerged under distinct

neural activity states: sparser, lower activity with increased variability in field and coupling parameters in the active condition; less sparse, higher activity with reduced variability in the passive condition. Thus, coupled with the previous results, this result indicates that the greater coupling variability in the active condition led to increased total entropy flow, making it comparable to the passive condition despite significantly sparser firing rate distributions.

Entropy flow per neuron and behavioral performance

To further elucidate how individual neurons increase total entropy flow in the active condition despite that a smaller fraction of neurons exhibits substantial firing rates (S1 Fig. S2 Fig., and S3 Fig.), we examined the relationship between the entropy flow and spike rates of individual neurons. As shown in Eqs. 13 and 14, the mean-field entropy flow can be decomposed into contributions from individual neurons. We computed the entropy flow of individual neurons under the active and passive conditions and compared them with their firing rates (Fig. 8A, mouse ID: 574078). The dotted lines connect the values for the active (red) and passive (blue) conditions (See S7 Fig for the result of all mice). We then investigated whether the change in the entropy flow by the behavioral conditions depends on the neuron’s firing rate. Figure 8B shows the relationship between the geometric mean spike rates of the two conditions (abscissa) and the difference in entropy flow (ordinate) for individual neurons. The difference was computed as ‘active’ - ‘passive,’ indicating that the positive value marks a larger entropy flow in the active condition. The positive Spearman rank correlation coefficient ($\rho = 0.22$) for this exemplary mouse suggests the tendency that neurons with higher spike rates contributed to increasing total entropy flow in the active condition, despite the summed entropy flow differences across all individual neurons being negative (-3.8331 for this mouse). However, significant variations in the rank correlations were

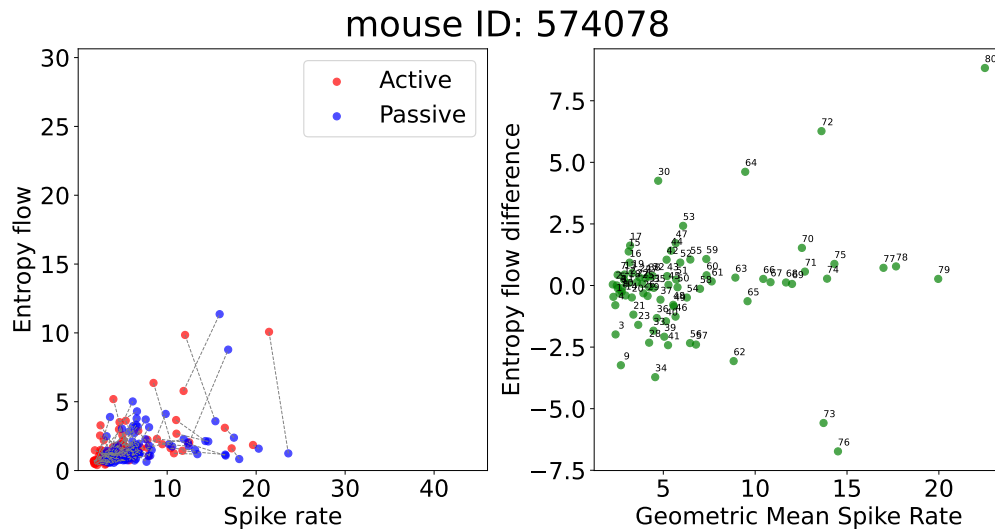


Fig 8. Relationship between spike rates and entropy flow for an example mouse. **A** Mean spike rate vs entropy flow per individual unit under the active and passive conditions (Mouse ID: 574078). Dashed lines connect values for the two conditions, highlighting behavioral state-dependent changes. **B** Geometric mean spike rate (abscissa) vs differences in entropy flow (ordinate) for individual units. The positive Spearman correlation coefficient ($\rho = 0.22$) suggests that units with higher spike rates increased entropy flow in the active condition.

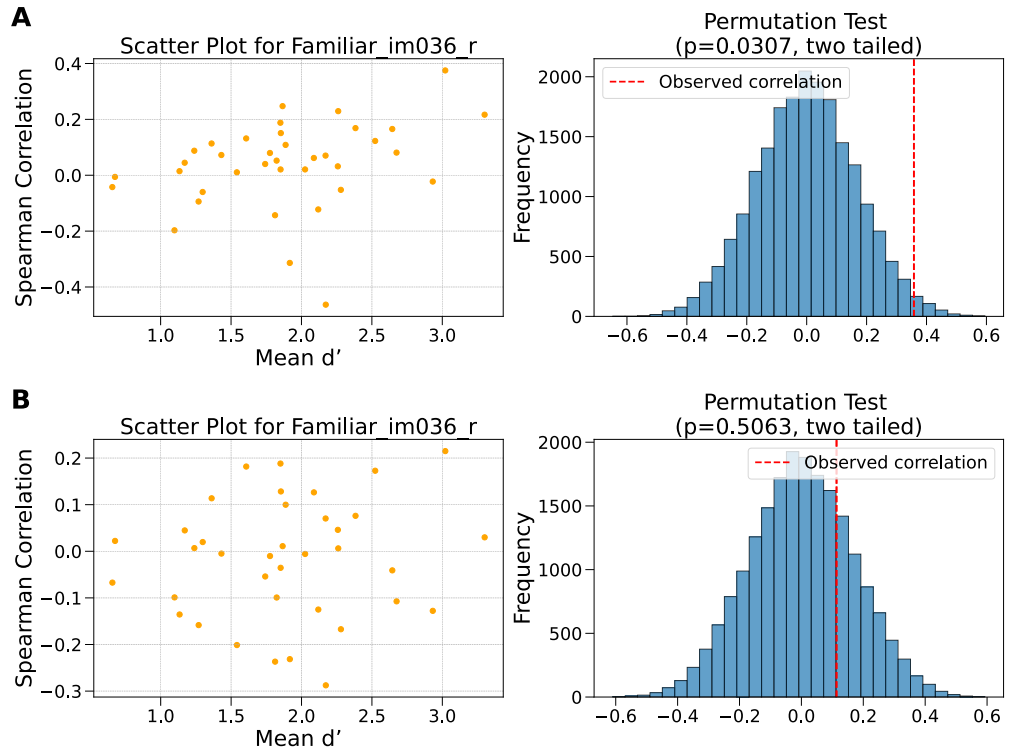


Fig 9. Relating the dependency of entropy flow change of individual units on firing rates with behavioral performance. **A** (Left) Scatter plot of behavioral performance (mean d' -prime) vs. the Spearman rank correlation between the geometric mean rate and entropy flow change of individual units (see Fig. 8). Each dot represents a single mouse. The dependency in this scatter plot was assessed again by the Spearman rank correlation coefficient, yielding $\rho = 0.3578$. (Right) A permutation test comparing the observed correlation value ρ with those obtained from the surrogate data. A statistically significant positive relationship was observed ($p = 0.0304$, two-tailed). The surrogate data was constructed by permuting the values of mean d' -prime. **B** Results for trial-shuffled data.

observed across mice (See S8 Fig for all mice).

Assuming that a fewer high-firing neurons in the sparsely active populations in the active condition play a critical role in sensory processing (i.e., sparse coding [56–58]) and that such sensory processing involves time-asymmetric causal patterns, we hypothesized that the above relationship between the spike rates and entropy flow change might be related to mice’s cognitive performance. To evaluate the task sensitivity of the mice, we used the primary behavioral metric, d' (*mean d' -prime*, see S2 Text for its definition). The scatter plot in Fig 9A illustrates the relationship between behavioral measures (mean d' -prime) and the rank correlation of entropy flow change with spike rates for all mice. The plot suggests a positive dependency between these two values ($\rho = 0.3578$ measured by the Spearman rank correlation). To confirm this result, we conducted the permutation test that compared the observed rank correlation of the scatter plot with those of the surrogate data constructed by permuting the values of mean d' -prime (Fig 9A Right). The result confirms the statistical significance of the positive correlation ($p = 0.0304$).

To corroborate that the result does not reflect estimation error in couplings, we analyzed trial-shuffled data, which showed no clear trend (Fig 9B). A permutation test

confirmed that the observed correlation yielded a non-significant p-value of 0.5063. This result confirms that the association between higher entropy flow and higher firing neurons in more task-sensitive mice was driven by significant changes in the coupling strengths between the active and passive conditions, rather than firing rate shifts or noise couplings. From these results, we conclude that despite reduced and sparser neuronal activity in the active condition, neurons with higher firing rates in more task-sensitive mice tend to increase entropy flow, exhibiting greater time-asymmetric activities. The effect of this selective enhancement of the entropy flow by higher-firing neurons was not observed at the population-activity level: Namely, shuffle-subtracted entropy flow in active or passive conditions and their changes across the conditions (Fig. 7C) vs d-prime did not show significant correlation (data not shown).

Discussion

This study presents a state-space kinetic Ising model for estimating nonstationary and nonequilibrium neural dynamics, alongside a mean-field method for entropy flow estimation. Through analysis of mouse V1 neurons, we identified distinct field and coupling distributions across behavioral conditions. These structural shifts influenced entropy flow compositions in V1 neurons, revealing correlations with behavioral performance.

To our knowledge, no inference methods have been proposed for time-dependent kinetic Ising models within the sequential Bayesian framework, which estimates parameters with uncertainty using optimized smoothness hyper-parameters (see [59] for Bayesian approach in a stationary case). While parameter estimation has often been considered under time-dependent fields with fixed couplings [34, 36] (see also [60, 61] for the equilibrium case), exceptions exist [35] that provide point estimates for time-varying couplings. These methods rely on mean-field equations relating equal-time and delayed correlations to coupling parameters, but estimating correlations at each time step is often infeasible in neuroscience data due to limited trial numbers in animal studies. Campajola et al. [62] proposed a point estimate of time-varying couplings using a score-driven method under the maximum likelihood principle but assumed all fields and couplings were uniformly scaled by a single time-varying parameter. In contrast, our state-space framework accommodates heterogeneous parameter dynamics and employs sequential Bayesian estimation with optimized smoothness parameters. These innovations are crucial for uncovering parameter variability’s impact on causal population dynamics and elucidating individual neuron’s contributions, which a homogeneous model cannot reveal.

Lower spike rates of V1 neurons observed during the active condition (see also [52]) contrast starkly with previous reports showing increased firing rates during active task engagement [63] or locomotion [64, 65]. Nevertheless, the diminished spike-rates found in the active condition (Fig. 5A and S1 Fig, S2 Fig) are in agreement with sparse population activity in processing natural images in mice V1 neurons [66, 67]. Further, active engagement broadened distributions of field and coupling parameters, possibly reflecting stronger and more diverse inputs from hidden neurons [68, 69]. These findings align with previously reported increased heterogeneous activities during the active condition and their correlation to behavioral performance [70]. Moreover, we found that, in the mice with higher task performance, neurons exhibiting higher spike rates increased entropy flow in active engagement (Fig. 9). These results indicate that, within the sparse population activity during the active condition, stronger time-asymmetric causal activity appeared in subset neurons with higher spike rates in competent mice, possibly elucidating detailed causal information flow in success or failure of sparse coding of visual images [56–58].

While our study highlights the utility of the state-space kinetic Ising model in capturing time-asymmetric dynamics, certain limitations remain. First, the estimated couplings capturing directed dynamics are statistical constructs and do not represent physiological synaptic connections. This difference arises partly from a mismatch between the nonlinearity of neurons in the kinetic Ising model (logistic/tanh activation function) and that of biological neurons [71, 72]. Future studies could incorporate more biologically plausible neuron models while maintaining the interpretability of thermodynamic properties in neural systems. Second, while we examined entropy flow in this study, assessing it alone provides an incomplete picture of the system. For example, increased entropy flow may occur when the system approaches criticality or a quasi-deterministic chaotic regime [31]. Future studies could incorporate additional metrics, such as conditional entropy, for a more precise characterization of neural population states. Third, this analysis primarily focused on short timescales related to stimulus responses, and further research is needed to assess the model’s ability to analyze longer-term dynamics, such as learning.

In summary, by developing a state-space kinetic Ising model that accounts for both non-stationary and nonequilibrium properties, we have demonstrated how task engagement modulates neuronal firing activity and coupling diversity. Our approach incorporates time-varying entropy flow estimation, revealing that time-asymmetric, irreversible activity emerges within sparsely active populations during task engagement—an effect correlated with the mouse’s behavioral performance. These findings underscore the utility of our approach, offering new insights into the thermodynamic underpinnings of neural computation.

Methods

Estimating time-varying parameters of the kinetic Ising model

We summarize the expectation-maximization algorithm for estimating the state-space kinetic Ising model with optimized hyper-parameters.

E-step Given the optimal parameter \mathbf{w} , we obtain the estimate of the state $\boldsymbol{\theta}$ given all the data available. When estimating the parameter $\boldsymbol{\theta}_t^i$ ($t = 0, 1, \dots, T$, $i = 1, \dots, N$) from the spike data \mathbf{x}_t ($t = 0, 1, \dots, T$), we first obtain the filter distribution by the sequentially applying the Bayes theorem:

$$p(\boldsymbol{\theta}_t | \mathbf{x}_{0:t}, \mathbf{w}) = \frac{p(\mathbf{x}_t | \boldsymbol{\theta}_t, \mathbf{x}_{0:t-1}, \mathbf{w}) p(\boldsymbol{\theta}_t | \mathbf{x}_{0:t-1}, \mathbf{w})}{p(\mathbf{x}_t | \mathbf{x}_{0:t-1}, \mathbf{w})} \quad (21)$$

Here the one-step prediction density is computed using the Chapman-Kolmogorov equation:

$$p(\boldsymbol{\theta}_t | \mathbf{x}_{0:t-1}, \mathbf{w}) = \prod_{i=1}^N \int p(\boldsymbol{\theta}_t^i | \boldsymbol{\theta}_{t-1}^i, \mathbf{Q}^i) p(\boldsymbol{\theta}_{t-1}^i | \mathbf{x}_{t-1}) d\boldsymbol{\theta}_{t-1}^i \quad (22)$$

By assuming that the filter density at the previous time step $t - 1$ is given by the Gaussian density with mean $\boldsymbol{\theta}_{t-1|t-1}^i$ and covariance $\mathbf{W}_{t-1|t-1}^i$. The one-step prediction density becomes the Gaussian density given by

$$p(\boldsymbol{\theta}_t | \mathbf{x}_{0:t-1}, \mathbf{w}) = \prod_{i=1}^N \exp \left[-\frac{1}{2} (\boldsymbol{\theta}_{t-1}^i - \boldsymbol{\theta}_{t|t-1}^i)^\top (\mathbf{W}_{t|t-1}^i)^{-1} (\boldsymbol{\theta}_{t-1}^i - \boldsymbol{\theta}_{t|t-1}^i) \right], \quad (23)$$

where the mean and covariance are given by $\boldsymbol{\theta}_{t|t-1}^i = \boldsymbol{\theta}_{t-1|t-1}^i$ and $\mathbf{W}_{t|t-1}^i = \mathbf{W}_{t-1|t-1}^i + \mathbf{Q}^i$. Then, the filter density is given by

$$p(\boldsymbol{\theta}_t | \mathbf{x}_{0:t}, \mathbf{w}) = \prod_{i=1}^N p(\boldsymbol{\theta}_t^i | \mathbf{x}_{0:t}, \mathbf{w}) \propto \prod_{i=1}^N \prod_{l=1}^L \exp \left[\theta_{i,t} x_{i,t}^l + \sum_{j=1}^N \theta_{ij,t} x_{it}^l x_{jt-1}^l - \psi(\boldsymbol{\theta}_t^i, \mathbf{x}_{t-1}^l) \right] \times \prod_{i=1}^N \exp \left[-\frac{1}{2} (\boldsymbol{\theta}_t^i - \boldsymbol{\theta}_{t|t-1}^i)^\top (\mathbf{W}_{t|t-1}^i)^{-1} (\boldsymbol{\theta}_t^i - \boldsymbol{\theta}_{t|t-1}^i) \right]. \quad (24)$$

Since this filter density is a concave function with respect to $\boldsymbol{\theta}_t^i$ for each neuron, we apply the Laplace approximation independently to the filter densities of individual neurons and obtain the approximate Gaussian distributions, where the mean is approximated by the MAP estimate:

$$\boldsymbol{\theta}_{t|t}^i = \arg \max_{\boldsymbol{\theta}_t^i} \log p(\boldsymbol{\theta}_t^i | \mathbf{x}_{0:t}, \mathbf{w}) \quad (25)$$

for $i = 1, \dots, N$, while the variance is approximated using the Hessian:

$$\mathbf{W}_{t|t}^i = \left[-\frac{\partial}{\partial \boldsymbol{\theta}_t^i} \frac{\partial \log p(\boldsymbol{\theta}_t^i | \mathbf{x}_{0:t}, \mathbf{w})}{\partial (\boldsymbol{\theta}_t^i)^\top} \Big|_{\boldsymbol{\theta}_t^i = \boldsymbol{\theta}_{t|t}^i} \right]^{-1} = \left[L\mathbf{G}^i(\boldsymbol{\theta}_{t|t}^i) + (\mathbf{W}_{t|t-1}^i)^{-1} \right]^{-1}, \quad (26)$$

where $\mathbf{G}^i \equiv \frac{\partial^2 \psi(\boldsymbol{\theta}_t^i, \mathbf{x}_{t-1}^l)}{\partial \boldsymbol{\theta}_t^i \partial (\boldsymbol{\theta}_t^i)^\top}$ is the Fisher information matrix with respect to $\boldsymbol{\theta}_t^i$ computed from the kinetic Ising model.

Next, we obtain the smoother density by recursively applying the formula. Because the filter density and state transitions are approximated by normal distributions, we follow the fixed-interval smoothing algorithm developed for the Gaussian distributions. In this method, the smoothed mean and covariance are recursively obtained by the following equations:

$$\boldsymbol{\theta}_{t-1|T}^i = \boldsymbol{\theta}_{t-1|t-1}^i + \mathbf{A}_{t-1}^i \left(\boldsymbol{\theta}_{t|T}^i - \boldsymbol{\theta}_{t|t}^i \right), \quad (27)$$

$$\mathbf{W}_{t-1|T}^i = \mathbf{W}_{t-1|t-1}^i + \mathbf{A}_{t-1}^i \left(\mathbf{W}_{t|T}^i - \mathbf{W}_{t|t}^i \right) \mathbf{A}_{t-1}^{i\top}, \quad (28)$$

$$\mathbf{A}_{t-1}^i = \mathbf{W}_{t-1|t-1}^i \left(\mathbf{W}_{t|t-1}^i \right)^{-1} \quad (29)$$

for $t = T, T-1, \dots, 2$.

M-step When optimizing the hyperparameter \mathbf{Q}^i in M-step, the update formula used is obtained as follows

$$\mathbf{Q}^i = \frac{1}{T-1} \sum_{t=2}^T \left(\boldsymbol{\theta}_{t|T}^i \boldsymbol{\theta}_{t|T}^{i\top} + \mathbf{W}_{t|T}^i - \boldsymbol{\theta}_{t-1|T}^i \boldsymbol{\theta}_{t|T}^{i\top} - \mathbf{W}_{t-1,t|T}^i - \boldsymbol{\theta}_{t|T}^i \boldsymbol{\theta}_{t-1|T}^{i\top} - \mathbf{W}_{t,t-1|T}^i + \boldsymbol{\theta}_{t-1|T}^i \boldsymbol{\theta}_{t-1|T}^{i\top} + \mathbf{W}_{t-1|T}^i \right). \quad (30)$$

We also note that the optimization of a diagonal of the form $\mathbf{Q}^i = \text{diag}[\lambda_0^i, \dots, \lambda_N^i]$ or $\mathbf{Q}^i = \lambda^i \mathbf{I}$ can be performed by taking diagonal and trace of the r.h.s of the equation above, respectively.

The convergence of the EM algorithm is assessed by computing the approximate log-likelihood function (Eq.6) using the Laplace approximation. Using Eqs. 1 and 23 in Eq.6, the approximate log-likelihood function for the hyperparameter \mathbf{w} is obtained as

$$\log[p(\mathbf{x}_{0:T}|\mathbf{w})] = \log[p(\mathbf{x}_0|\mathbf{w})] + \sum_{t=2}^T \sum_{i=1}^N \left[\frac{1}{2} \log |\mathbf{W}_{t|t}^i| - \frac{1}{2} \log |\mathbf{W}_{t|t-1}^i| + q(\boldsymbol{\theta}_{t|t}^i) \right]. \quad (31)$$

Mean-field approximation of the entropy flow

Here we extend the mean-field approximation method developed for the steady-state kinetic Ising model [37] to make it applicable to non-stationarity systems.

First, σ_t^{flow} can be decomposed as follows by introducing the forward and backward conditional entropies:

$$\sigma_t^{\text{flow}} = -\sigma_t^{\text{forward}} + \sigma_t^{\text{backward}}, \quad (32)$$

where

$$\sigma_t^{\text{forward}} = - \sum_{\mathbf{x}_t, \mathbf{x}_{t-1}} p(\mathbf{x}_t, \mathbf{x}_{t-1}) \log p(\mathbf{x}_t | \mathbf{x}_{t-1}), \quad (33)$$

$$\sigma_t^{\text{backward}} = - \sum_{\mathbf{x}_t, \mathbf{x}_{t-1}} p(\mathbf{x}_t, \mathbf{x}_{t-1}) \log p(\mathbf{x}_{t-1} | \mathbf{x}_t). \quad (34)$$

We calculate these conditional entropies using the Gaussian approximation as follows. First, $\sigma_t^{\text{forward}}$ can be represented as

$$\begin{aligned} \sigma_t^{\text{forward}} &= - \sum_{\mathbf{x}_t, \mathbf{x}_{t-1}} \sum_{\mathbf{x}_{t-2}} p(\mathbf{x}_t | \mathbf{x}_{t-1}) p(\mathbf{x}_{t-1} | \mathbf{x}_{t-2}) p(\mathbf{x}_{t-2}) \log p(\mathbf{x}_t | \mathbf{x}_{t-1}) \\ &= - \sum_{\mathbf{x}_{t-1}} \sum_{\mathbf{x}_{t-2}} p(\mathbf{x}_{t-1} | \mathbf{x}_{t-2}) p(\mathbf{x}_{t-2}) \sum_{\mathbf{x}_t} p(\mathbf{x}_t | \mathbf{x}_{t-1}) \log p(\mathbf{x}_t | \mathbf{x}_{t-1}) \end{aligned} \quad (35)$$

Here, we replace $p(\mathbf{x}_{t-1} | \mathbf{x}_{t-2})$ with an independent model $Q(\mathbf{x}_{t-1})$ defined as

$$Q(\mathbf{x}_{t-1}) = \prod_i Q(x_{i,t-1}) = \prod_i \frac{e^{x_{i,t-1} \theta_{i,t-1}^0}}{1 + e^{\theta_{i,t-1}^0}}, \quad (36)$$

where $\theta_{i,t-1}^0$ is the parameter of the independent model for the i -th neuron. Then, $\sigma_t^{\text{forward}}$ is approximated as

$$\sigma_t^{\text{forward}} \simeq - \sum_{\mathbf{x}_{t-1}} Q(\mathbf{x}_{t-1}) \sum_{\mathbf{x}_t} p(\mathbf{x}_t | \mathbf{x}_{t-1}) \log p(\mathbf{x}_t | \mathbf{x}_{t-1}). \quad (37)$$

The conditional probability is written as

$$p(\mathbf{x}_t | \mathbf{x}_{t-1}) = \prod_i p(x_{i,t} | \mathbf{x}_{t-1}), \quad (38)$$

where

$$p(x_{i,t} | \mathbf{x}_{t-1}) = \frac{e^{x_{i,t} h_{i,t}(\mathbf{x}_{t-1})}}{1 + e^{h_{i,t}(\mathbf{x}_{t-1})}}, \quad (39)$$

with

$$h_{i,t}(\mathbf{x}_{t-1}) = \theta_{i,t} + \sum_j \theta_{ij,t} x_{j,t-1}. \quad (40)$$

Note that the expectation of $x_{i,t}$ is given by

$$\begin{aligned} r(h_{i,t}(\mathbf{x}_{t-1})) &= \sum_{x_{i,t}} x_{i,t} p(x_{i,t} | \mathbf{x}_{t-1}) \\ &= \frac{1}{1 + e^{-h_{i,t}(\mathbf{x}_{t-1})}}. \end{aligned} \quad (41)$$

Using $r(h_{i,t}(\mathbf{x}_{t-1}))$, we have

$$p(x_{i,t} = 1 | \mathbf{x}_{t-1}) = \frac{e^{h_{i,t}(\mathbf{x}_{t-1})}}{1 + e^{h_{i,t}(\mathbf{x}_{t-1})}} = r(h_{i,t}(\mathbf{x}_{t-1})), \quad (42)$$

$$p(x_{i,t} = 0 | \mathbf{x}_{t-1}) = \frac{1}{1 + e^{h_{i,t}(\mathbf{x}_{t-1})}} = 1 - r(h_{i,t}(\mathbf{x}_{t-1})). \quad (43)$$

Then the forward conditional entropy becomes

$$\begin{aligned} \sigma_t^{\text{forward}} &\simeq - \sum_{\mathbf{x}_{t-1}} Q(\mathbf{x}_{t-1}) \sum_{\mathbf{x}_t} p(\mathbf{x}_t | \mathbf{x}_{t-1}) \log p(\mathbf{x}_t | \mathbf{x}_{t-1}) \\ &= - \sum_{\mathbf{x}_{t-1}} Q(\mathbf{x}_{t-1}) \sum_i \sum_{x_{i,t}} p(x_{i,t} | \mathbf{x}_{t-1}) \log p(x_{i,t} | \mathbf{x}_{t-1}) \\ &= \sum_{\mathbf{x}_{t-1}} Q(\mathbf{x}_{t-1}) \sum_i \chi(h_{i,t}(\mathbf{x}_{t-1})), \end{aligned} \quad (44)$$

where

$$\begin{aligned} \chi(h_{i,t}(\mathbf{x}_{t-1})) &\equiv - \sum_{x_{i,t}} p(x_{i,t} | \mathbf{x}_{t-1}) \log p(x_{i,t} | \mathbf{x}_{t-1}) \\ &= -r(h_{i,t}(\mathbf{x}_{t-1})) \log r(h_{i,t}(\mathbf{x}_{t-1})) \\ &\quad - (1 - r(h_{i,t}(\mathbf{x}_{t-1}))) \log(1 - r(h_{i,t}(\mathbf{x}_{t-1}))) \end{aligned} \quad (45)$$

Furthermore, by defining $\Gamma_{i,t}$,

$$\Gamma_{i,t} = \sum_{\mathbf{x}_{t-1}} Q(\mathbf{x}_{t-1}) \chi(h_{i,t}(\mathbf{x}_{t-1})), \quad (46)$$

$\sigma_t^{\text{forward}}$ can be summarized as

$$\sigma_t^{\text{forward}} = \sum_i \Gamma_{i,t}. \quad (47)$$

Here, we approximate $\Gamma_{i,t}$ by a Gaussian distribution based on the central limit theorem for a collection of independent binary signals. Specifically, by using $\mathcal{D}_z = \frac{dz}{\sqrt{2\pi}} \exp(-\frac{1}{2}z^2)$, $\Gamma_{i,t}$ is approximated as

$$\Gamma_{i,t} = \sum_{\mathbf{x}_{t-1}} Q(\mathbf{x}_{t-1}) \chi(h_{i,t}(\mathbf{x}_{t-1})) \approx \int \mathcal{D}_z \chi_{i,t}(g_{i,t} + z\sqrt{\Delta_{i,t}}) \quad (48)$$

where $g_{i,t}$ and $\Delta_{i,t}$ are the mean of $h_{i,t}(\mathbf{x}_{t-1})$ given by

$$g_{i,t} \equiv \theta_{i,t} + \sum_j \theta_{ij,t} m_{j,t-1}, \quad (49)$$

$$\Delta_{i,t} \equiv \text{Var}[h_{i,t}] = \sum_j \theta_{ij,t}^2 m_{j,t-1} (1 - m_{j,t-1}). \quad (50)$$

Here, $m_{i,t}$ ($t = 1, \dots, T$) is the mean-field approximation of $x_{i,t}$ obtained by the Gaussian approximation method assuming independent activity of neurons at $t - 1$:

$$\begin{aligned}
m_{i,t} &\equiv \sum_{\mathbf{x}_t, \mathbf{x}_{t-1}} x_{i,t} p(\mathbf{x}_t | \mathbf{x}_{t-1}) p(\mathbf{x}_{t-1}) \\
&\simeq \sum_{\mathbf{x}_t, \mathbf{x}_{t-1}} x_{i,t} p(\mathbf{x}_t | \mathbf{x}_{t-1}) Q(\mathbf{x}_{t-1}) \\
&= \sum_{\mathbf{x}_{t-1}} Q(\mathbf{x}_{t-1}) \sum_{\mathbf{x}_t} x_{i,t} p(\mathbf{x}_t | \mathbf{x}_{t-1}) \\
&= \sum_{\mathbf{x}_{t-1}} Q(\mathbf{x}_{t-1}) r(h_{i,t}(\mathbf{x}_{t-1}))
\end{aligned} \tag{51}$$

Applying the Gaussian approximation to $h_{i,t}(\mathbf{x}_{t-1})$, $m_{i,t}$ is recursively computed as

$$m_{i,t} \simeq \sum_{\mathbf{x}_{t-1}} r(h_{i,t}(\mathbf{x}_{t-1})) Q(\mathbf{x}_{t-1}) \approx \int \mathcal{D}_z r(g_{i,t} + z\sqrt{\Delta_{i,t}}), \tag{52}$$

for $t = 1, \dots, T$, using Eqs. 49 and 50, which are functions of $m_{i,t-1}$. Here $m_{i,1}$ was computed using nominal values of $m_{i,0}$ ($i = 1, \dots, N$). In the simulation and empirical analyses, we used spiking probability averaged over all time steps and trials for each neuron as $m_{i,0}$.

Next, we approximate $\sigma_t^{\text{backward}}$. It is computed as

$$\begin{aligned}
\sigma_t^{\text{backward}} &= - \sum_{\mathbf{x}_t, \mathbf{x}_{t-1}} p(\mathbf{x}_t, \mathbf{x}_{t-1}) \log p(\mathbf{x}_{t-1} | \mathbf{x}_t) \\
&= - \sum_{\mathbf{x}_{t-2}} p(\mathbf{x}_{t-2}) \sum_{\mathbf{x}_t, \mathbf{x}_{t-1}} p(\mathbf{x}_t | \mathbf{x}_{t-1}) p(\mathbf{x}_{t-1} | \mathbf{x}_{t-2}) \log p(\mathbf{x}_{t-1} | \mathbf{x}_t) \\
&= - \sum_{\mathbf{x}_t, \mathbf{x}_{t-1}} \sum_{\mathbf{x}_{t-2}} p(\mathbf{x}_t | \mathbf{x}_{t-1}) p(\mathbf{x}_{t-1} | \mathbf{x}_{t-2}) p(\mathbf{x}_{t-2}) \sum_i [x_{i,t-1} h_{i,t}(\mathbf{x}_t) - \psi(h_{i,t}(\mathbf{x}_t))] \\
&= - \sum_{\mathbf{x}_{t-2}} \sum_{\mathbf{x}_{t-1}} p(\mathbf{x}_{t-1} | \mathbf{x}_{t-2}) p(\mathbf{x}_{t-2}) \sum_{\mathbf{x}_t} p(\mathbf{x}_t | \mathbf{x}_{t-1}) \sum_i [x_{i,t-1} h_{i,t}(\mathbf{x}_t) - \psi(h_{i,t}(\mathbf{x}_t))]
\end{aligned} \tag{53}$$

We note that

$$\begin{aligned}
\sum_{\mathbf{x}_{t-1}} p(\mathbf{x}_{t-1} | \mathbf{x}_{t-2}) &= \sum_{\mathbf{x}_{t-1}} \prod_i p(x_{i,t-1} | \mathbf{x}_{t-2}) \\
&= \sum_{x_{1,t-1}} \sum_{x_{2,t-1}} \cdots \sum_{x_{N,t-1}} \prod_i p(x_{i,t-1} | \mathbf{x}_{t-2}) \\
&= \prod_i \sum_{x_{i,t-1}} p(x_{i,t-1} | \mathbf{x}_{t-2}).
\end{aligned} \tag{54}$$

We approximate the following probabilities by independent distributions.

$$p(\mathbf{x}_{t-2}) = Q(\mathbf{x}_{t-2}), \tag{55}$$

$$p(\mathbf{x}_t | \mathbf{x}_{t-1}) = Q(\mathbf{x}_t). \tag{56}$$

Using these equations, $\sigma_t^{\text{backward}}$ can be approximated as follows:

$$\begin{aligned}
\sigma_t^{\text{backward}} &\simeq - \sum_{\mathbf{x}_{t-2}} \sum_{\mathbf{x}_{t-1}} p(\mathbf{x}_{t-1}|\mathbf{x}_{t-2}) Q(\mathbf{x}_{t-2}) \sum_{\mathbf{x}_t} Q(\mathbf{x}_t) \sum_i [x_{i,t-1} h_{i,t}(\mathbf{x}_t) - \psi(h_{i,t}(\mathbf{x}_t))] \\
&= - \sum_{\mathbf{x}_{t-2}} Q(\mathbf{x}_{t-2}) \sum_{\mathbf{x}_t} Q(\mathbf{x}_t) \sum_{\mathbf{x}_{t-1}} p(\mathbf{x}_{t-1}|\mathbf{x}_{t-2}) \sum_i [x_{i,t-1} h_{i,t}(\mathbf{x}_t) - \psi(h_{i,t}(\mathbf{x}_t))] \\
&= - \sum_{\mathbf{x}_t} Q(\mathbf{x}_t) \sum_{\mathbf{x}_{t-2}} Q(\mathbf{x}_{t-2}) \sum_i [r(h_{i,t-1}(\mathbf{x}_{t-2})) h_{i,t}(\mathbf{x}_t) - \psi(h_{i,t}(\mathbf{x}_t))] \\
&= - \sum_i \sum_{\mathbf{x}_t} Q(\mathbf{x}_t) [m_{i,t-1} h_{i,t}(\mathbf{x}_t) - \psi(h_{i,t}(\mathbf{x}_t))], \tag{57}
\end{aligned}$$

where we used Eqs. 41, 54 to obtain the third equality and Eq. 51 to obtain the last result. By defining

$$\phi_i(h_{i,t}(\mathbf{x}_t)) = -(m_{i,t-1} h_{i,t}(\mathbf{x}_t) - \psi(h_{i,t}(\mathbf{x}_t))), \tag{58}$$

the backward conditional entropy is obtained by the Gaussian integral:

$$\begin{aligned}
\sigma_t^{\text{backward}} &= \sum_i \sum_{\mathbf{x}_t} Q(\mathbf{x}_t) \phi_i(h_{i,t}(\mathbf{x}_t)) \\
&\approx \sum_i \int \mathcal{D}_z \phi_i(g_{i,t} + z\sqrt{\Delta_{i,t}}). \tag{59}
\end{aligned}$$

An alternative approach to obtain the backward conditional entropy is given in S1 Text.

Supporting information

S1 text. An alternative calculation of the backward conditional entropy

S2 text. The d-prime measure

S1 Fig. Spike-rate dynamics and distributions for mice 1-18 Spike-rate dynamics and distributions under the active (red) and passive (blue) conditions. The presentation styles for each mouse follow Fig. 5A. The mice were listed in descending order of behavioral performance measured by d-prime. See Fig. S2 Fig for the remaining mice.

S2 Fig. Spike-rate dynamics and distributions for mice 19-37 The same as in S1 Fig but for the remaining 19 mice.

S3 Fig. Comparison of mean spike rates and coefficient of variation in the active and passive conditions. **A** Mean spiking probability across all bins, trials, and neurons in active and passive conditions. Each line represents the same mouse. Neurons showed significantly lower firing rates in the active condition ($p = 1.556 \times 10^{-8}$, Wilcoxon signed-rank test). **B** Coefficient of variations (CVs) of the firing rate distributions, a measure of sparseness, in the active and passive conditions. CV was significantly higher in the active condition ($p = 8.35 \times 10^{-8}$, Wilcoxon signed-rank test).

S4 Fig. Estimated neural dynamics under active and passive conditions in shuffled data of mouse 574078. Presentation style follows Fig. 5.

S5 Fig. Time courses of entropy flow and mean spike rates for each mouse under active and passive conditions. Each subplot represents the dynamics of an individual mouse. Solid lines are entropy flows (red for active, blue for passive) while dashed lines represent the average population spike rate (red for active, blue for passive).

S6 Fig. Comparison of significant parameter variabilities and coupling asymmetry with entropy flow for all mice. Each row represents comparisons of significant parameter variabilities and coupling asymmetry (calculated by subtracting the shuffled-data estimate of the variance from the original-data estimate) and their relationship to the shuffle-subtracted entropy flow. **A, B, C** “ Δ active” (significant changes in the field, coupling variabilities, and coupling asymmetry) versus the shuffle-subtracted entropy flow in the active state. **D, E, F** “ Δ passive” versus the shuffle-subtracted entropy flow in the passive state.

S7 Fig. Distributions of mean spike rates and entropy flows for all mice. Each point represents a unit under active (red) and passive (blue) conditions. Dashed lines connect the same units.

S8 Fig. Entropy flow difference versus mean spike counts for all mice. Each subplot represents an individual mouse. The x-axis is the geometric mean of spike counts under active and passive conditions while the y-axis is the entropy flow difference between these conditions. Each data point corresponds to one neuron with labels indicating neuron indices.

Data availability

We used publicly available “Allen Brain Observatory: Visual Behavior Neuropixels” dataset provided by Allen Institute for Brain Science:
<https://portal.brain-map.org/circuits-behavior/visual-behavior-neuropixels>.

Code availability

The code used to analyze the data is available in the Github repository:
https://github.com/KenIshihara-17171ken/Non_equ.

Acknowledgments

This work was supported by JSPS KAKENHI Grant Number JP 20K11709, 21H05246, 24K21518.

References

1. Schrödinger E. What is Life?: The Physical Aspect of the Living Cell; 1944.
2. Prigogine I, Stengers I. Order Out of Chaos: Man’s New Dialogue with Nature. Bantam new age books. Bantam Books; 1984.
3. Kondepudi D, Prigogine I. Modern thermodynamics: from heat engines to dissipative structures. John wiley & sons; 2014.

4. Eigen M, Winkler R. *Laws of the game: how the principles of nature govern chance*. vol. 10. Princeton University Press; 1993.
5. Schneider ED, Kay JJ. Life as a manifestation of the second law of thermodynamics. *Mathematical and computer modelling*. 1994;19(6-8):25–48.
6. Schnakenberg J. Network theory of microscopic and macroscopic behavior of master equation systems. *Reviews of Modern Physics*. 1976;48(4):571–585. doi:10.1103/RevModPhys.48.571.
7. Crooks GE. Entropy production fluctuation theorem and the nonequilibrium work relation for free energy differences. *Physical Review E*. 1999;60(3):2721.
8. Evans DJ, Searles DJ. The fluctuation theorem. *Advances in Physics*. 2002;51(7):1529–1585.
9. Seifert U. Stochastic thermodynamics, fluctuation theorems and molecular machines. *Reports on progress in physics*. 2012;75(12):126001.
10. Churchland MM, Cunningham JP, Kaufman MT, Foster JD, Nuyujukian P, Ryu SI, et al. Neural population dynamics during reaching. *Nature*. 2012;487(7405):51–56.
11. Kuzmina E, Kriukov D, Lebedev M. Neuronal travelling waves explain rotational dynamics in experimental datasets and modelling. *Scientific Reports*. 2024;14(1):3566.
12. Skaggs WE, McNaughton BL. Replay of neuronal firing sequences in rat hippocampus during sleep following spatial experience. *Science*. 1996;271(5257):1870–1873.
13. Lee AK, Wilson MA. Memory of sequential experience in the hippocampus during slow wave sleep. *Neuron*. 2002;36(6):1183–1194.
14. Harris KD, Csicsvari J, Hirase H, Dragoi G, Buzsáki G. Organization of cell assemblies in the hippocampus. *Nature*. 2003;424(6948):552–556.
15. Hebb DO. *The Organization of Behavior: A Neuropsychological Theory*. New York: Wiley; 1949.
16. Abeles M. *Corticonics: Neural circuits of the cerebral cortex*. Cambridge University Press; 1991.
17. Diesmann M, Gewaltig MO, Aertsen A. Stable propagation of synchronous spiking in cortical neural networks. *Nature*. 1999;402(6761):529–533.
18. Harris KD. Neural signatures of cell assembly organization. *Nature reviews neuroscience*. 2005;6(5):399–407.
19. Izhikevich EM. Polychronization: computation with spikes. *Neural computation*. 2006;18(2):245–282.
20. Ito S, Oizumi M, Amari Si. Unified framework for the entropy production and the stochastic interaction based on information geometry. *Physical Review Research*. 2020;2(3):033048.
21. Yang YJ, Qian H. Unified formalism for entropy production and fluctuation relations. *Physical Review E*. 2020;101(2):022129.

22. Perl YS, Bocaccio H, Pallavicini C, Pérez-Ipiña I, Laureys S, Laufs H, et al. Nonequilibrium brain dynamics as a signature of consciousness. *Physical Review E*. 2021;104(1):014411.
23. de la Fuente LA, Zamberlan F, Bocaccio H, Kringelbach M, Deco G, Perl YS, et al. Temporal irreversibility of neural dynamics as a signature of consciousness. *Cerebral Cortex*. 2022;doi:10.1093/cercor/bhac177.
24. Gilson M, Tagliazucchi E, Cofré R. Entropy production of multivariate Ornstein-Uhlenbeck processes correlates with consciousness levels in the human brain. *Physical Review E*. 2023;107(2):024121.
25. Sekizawa D, Ito S, Oizumi M. Decomposing thermodynamic dissipation of linear Langevin systems via oscillatory modes and its application to neural dynamics. *Physical Review X*. 2024;14(4):041003.
26. Lynn CW, Cornblath EJ, Papadopoulos L, Bertolero MA, Bassett DS. Broken detailed balance and entropy production in the human brain. *Proceedings of the National Academy of Sciences*. 2021;118(47).
27. Crisanti A, Sompolinsky H. Dynamics of spin systems with randomly asymmetric bonds: Langevin dynamics and a spherical model. *Physical Review A*. 1987;36(10):4922.
28. Crisanti A, Sompolinsky H. Dynamics of spin systems with randomly asymmetric bonds: Ising spins and Glauber dynamics. *Physical Review A*. 1988;37(12):4865.
29. Schneidman E, Berry MJ, Segev R, Bialek W. Weak pairwise correlations imply strongly correlated network states in a neural population. *Nature*. 2006;440(7087):1007–1012.
30. Tkačik G, Mora T, Marre O, Amodei D, Palmer SE, Berry MJ, et al. Thermodynamics and signatures of criticality in a network of neurons. *Proceedings of the National Academy of Sciences*. 2015;112(37):11508–11513.
31. Aguilera M, Igarashi M, Shimazaki H. Nonequilibrium thermodynamics of the asymmetric Sherrington-Kirkpatrick model. *Nature Communications*. 2023;14(1):3685.
32. Kappen H, Spanjers J. Mean field theory for asymmetric neural networks. *Physical Review E*. 2000;61(5):5658.
33. Roudi Y, Hertz J. Dynamical TAP equations for non-equilibrium Ising spin glasses. *Journal of Statistical Mechanics: Theory and Experiment*. 2011;2011(03):P03031.
34. Roudi Y, Hertz J. Mean field theory for nonequilibrium network reconstruction. *Physical review letters*. 2011;106(4):048702.
35. Mézard M, Sakellariou J. Exact mean-field inference in asymmetric kinetic Ising systems. *Journal of Statistical Mechanics: Theory and Experiment*. 2011;2011(07):L07001.
36. Sakellariou J, Roudi Y, Mezard M, Hertz J. Effect of coupling asymmetry on mean-field solutions of the direct and inverse Sherrington-Kirkpatrick model. *Philosophical Magazine*. 2012;92(1-3):272–279.

37. Aguilera M, Moosavi SA, Shimazaki H. A unifying framework for mean-field theories of asymmetric kinetic Ising systems. *Nature communications*. 2021;12(1):1197.
38. Brown EN, Frank LM, Tang D, Quirk MC, Wilson MA. A statistical paradigm for neural spike train decoding applied to position prediction from ensemble firing patterns of rat hippocampal place cells. *Journal of Neuroscience*. 1998;18(18):7411–7425.
39. Yu BM, Cunningham JP, Santhanam G, Ryu S, Shenoy KV, Sahani M. Gaussian-process factor analysis for low-dimensional single-trial analysis of neural population activity. *Advances in neural information processing systems*. 2008;21.
40. Shimazaki H, Amari Si, Brown EN, Grun S. State-space analysis on time-varying correlations in parallel spike sequences. In: *2009 IEEE International Conference on Acoustics, Speech and Signal Processing*. IEEE; 2009. p. 3501–3504.
41. Shimazaki H, Amari Si, Brown EN, Grün S. State-space analysis of time-varying higher-order spike correlation for multiple neural spike train data. *PLoS computational biology*. 2012;8(3):e1002385.
42. Donner C, Obermayer K, Shimazaki H. Approximate inference for time-varying interactions and macroscopic dynamics of neural populations. *PLoS computational biology*. 2017;13(1):e1005309.
43. Gaudreault J, Shimazaki H. State-space analysis of an Ising model reveals contributions of pairwise interactions to sparseness, fluctuation, and stimulus coding of monkey V1 neurons. In: *Artificial Neural Networks and Machine Learning–ICANN 2018, Proceedings, Part III 27*. Springer; 2018. p. 641–651.
44. Gaudreault J, Saxena A, Shimazaki H. Online estimation of multiple dynamic graphs in pattern sequences. In: *2019 International Joint Conference on Neural Networks (IJCNN)*. IEEE; 2019. p. 1–8.
45. Shumway RH, Stoffer DS. An approach to time series smoothing and forecasting using the EM algorithm. *Journal of time series analysis*. 1982;3(4):253–264.
46. Smith AC, Brown EN. Estimating a state-space model from point process observations. *Neural computation*. 2003;15(5):965–991.
47. Dempster AP, Laird NM, Rubin DB. Maximum likelihood from incomplete data via the EM algorithm. *Journal of the royal statistical society: series B (methodological)*. 1977;39(1):1–22.
48. Wolpert DH, Korbel J, Lynn CW, Tasnim F, Grochow JA, Kardeş G, et al. Is stochastic thermodynamics the key to understanding the energy costs of computation? *Proceedings of the National Academy of Sciences*. 2024;121(45):e2321112121.
49. Gaspard P. Time-reversed dynamical entropy and irreversibility in Markovian random processes. *Journal of statistical physics*. 2004;117:599–615.
50. Cofré R, Videla L, Rosas F. An introduction to the non-equilibrium steady states of maximum entropy spike trains. *Entropy*. 2019;21(9):884.
51. Igarashi M. Entropy production for discrete-time markov processes. *arXiv:220507214*. 2022;.

52. Siegle JH, Jia X, Durand S, Gale S, Bennett C, Graddis N, et al. Survey of spiking in the mouse visual system reveals functional hierarchy. *Nature*. 2021;592(7852):86–92.
53. Nitzan N, Bennett C, Movshon JA, Olsen SR, Buzsáki G. Mixing novel and familiar cues modifies representations of familiar visual images and affects behavior. *Cell reports*. 2024;43(8).
54. Ito S, Piet A, Bennett C, Durand S, Belski H, Garrett M, et al. Coordinated changes in a cortical circuit sculpt effects of novelty on neural dynamics. *Cell reports*. 2024;43(9).
55. Rolls ET, Tovee MJ. Sparseness of the neuronal representation of stimuli in the primate temporal visual cortex. *Journal of neurophysiology*. 1995;73(2):713–726.
56. Olshausen BA, Field DJ. Emergence of simple-cell receptive field properties by learning a sparse code for natural images. *Nature*. 1996;381(6583):607–609.
57. Olshausen BA, Field DJ. Sparse coding with an overcomplete basis set: A strategy employed by V1? *Vision research*. 1997;37(23):3311–3325.
58. Foldiak P. Sparse coding in the primate cortex. *The handbook of brain theory and neural networks*. 2003; p. 895–898.
59. Donner C, Opper M. Inverse Ising problem in continuous time: A latent variable approach. *Physical Review E*. 2017;96(6):062104.
60. Delamare G, Ferrari U. Time-dependent maximum entropy model for populations of retinal ganglion cells. In: *Physical Sciences Forum*. vol. 5. MDPI; 2022. p. 31.
61. Granot-Atedgi E, Tkačik G, Segev R, Schneidman E. Stimulus-dependent maximum entropy models of neural population codes. *PLoS computational biology*. 2013;9(3):e1002922.
62. Campajola C, Gangi DD, Lillo F, Tantari D. Modelling time-varying interactions in complex systems: the Score Driven Kinetic Ising Model. *Scientific Reports*. 2022;12(1):19339.
63. Pho GN, Goard MJ, Woodson J, Crawford B, Sur M. Task-dependent representations of stimulus and choice in mouse parietal cortex. *Nature communications*. 2018;9(1):2596.
64. Dadarlat MC, Stryker MP. Locomotion enhances neural encoding of visual stimuli in mouse V1. *Journal of Neuroscience*. 2017;37(14):3764–3775.
65. Christensen AJ, Pillow JW. Reduced neural activity but improved coding in rodent higher-order visual cortex during locomotion. *Nature communications*. 2022;13(1):1676.
66. Froudarakis E, Berens P, Ecker AS, Cotton RJ, Sinz FH, Yatsenko D, et al. Population code in mouse V1 facilitates readout of natural scenes through increased sparseness. *Nature neuroscience*. 2014;17(6):851–857.
67. Yoshida T, Ohki K. Natural images are reliably represented by sparse and variable populations of neurons in visual cortex. *Nature communications*. 2020;11(1):872.
68. Renart A, Machens CK. Variability in neural activity and behavior. *Current opinion in neurobiology*. 2014;25:211–220.

69. Brinkman BA, Rieke F, Shea-Brown E, Buice MA. Predicting how and when hidden neurons skew measured synaptic interactions. *PLoS computational biology*. 2018;14(10):e1006490.
70. Montijn JS, Goltstein PM, Pennartz CM. Mouse V1 population correlates of visual detection rely on heterogeneity within neuronal response patterns. *Elife*. 2015;4:e10163.
71. Shomali SR, Rasuli SN, Ahmadabadi MN, Shimazaki H. Uncovering hidden network architecture from spiking activities using an exact statistical input-output relation of neurons. *Communications Biology*. 2023;6(1):169.
72. Rodríguez-Domínguez U, Shimazaki H. Alternating Shrinking Higher-order Interactions for Sparse Neural Population Activity. arXiv preprint arXiv:230813257. 2023;.
73. Hautus MJ, Macmillan NA, Creelman CD. *Detection theory: A user's guide*. Routledge; 2021.

Supporting Information

Ken Ishihara

*Graduate School of Life Sciences, Hokkaido University, Sapporo, Japan
Center for Human Nature, Artificial Intelligence,
and Neuroscience (CHAIN), Hokkaido University, Sapporo, Japan*

Hideaki Shimazaki

*Graduate School of Informatics, Kyoto University, Kyoto, Japan
Center for Human Nature, Artificial Intelligence,
and Neuroscience (CHAIN), Hokkaido University, Sapporo, Japan*

1 S1 text. An alternative calculation of the backward conditional entropy

Here we give an alternative approach to obtain the backward conditional entropy to the one given in Methods. The result gives an identical approximate solution.

Under the approximation of the following probabilities by independent distributions:

$$p(\mathbf{x}_{t-2}) = Q(\mathbf{x}_{t-2}), \quad (60)$$

$$p(\mathbf{x}_t | \mathbf{x}_{t-1}) = Q(\mathbf{x}_t). \quad (61)$$

the backward conditional entropy is approximated as

$$\begin{aligned} \sigma_t^{\text{backward}} &= - \sum_{\mathbf{x}_{t-2}} \sum_{\mathbf{x}_{t-1}} p(\mathbf{x}_{t-1} | \mathbf{x}_{t-2}) p(\mathbf{x}_{t-2}) \sum_{\mathbf{x}_t} p(\mathbf{x}_t | \mathbf{x}_{t-1}) \sum_i [x_{i,t-1} h_{i,t}(\mathbf{x}_t) - \psi(h_{i,t}(\mathbf{x}_t))] \\ &= - \sum_{\mathbf{x}_{t-2}} \sum_{\mathbf{x}_{t-1}} p(\mathbf{x}_{t-1} | \mathbf{x}_{t-2}) Q(\mathbf{x}_{t-2}) \sum_{\mathbf{x}_t} Q(\mathbf{x}_t) \sum_i [x_{i,t-1} h_{i,t}(\mathbf{x}_t) - \psi(h_{i,t}(\mathbf{x}_t))] \\ &= - \sum_i \sum_{x_{i,t-1}} \sum_{\mathbf{x}_{t-2}} p(x_{i,t-1} | \mathbf{x}_{t-2}) Q(\mathbf{x}_{t-2}) \sum_{\mathbf{x}_t} Q(\mathbf{x}_t) [x_{i,t-1} h_{i,t}(\mathbf{x}_t) - \psi(h_{i,t}(\mathbf{x}_t))] \end{aligned} \quad (62)$$

and define $\tilde{\phi}_i(x_{i,t})$ as

$$\tilde{\phi}_i(x_{i,t-1}) = \sum_{\mathbf{x}_t} Q(\mathbf{x}_t) [x_{i,t-1} h_{i,t}(\mathbf{x}_t) - \psi(h_{i,t}(\mathbf{x}_t))], \quad (63)$$

Using

$$\gamma(h_{i,t}) = x_{i,t-1} h_{i,t} - \psi(h_{i,t}), \quad (64)$$

$\tilde{\phi}_i(x_{i,t})$ can be approximated as

$$\begin{aligned} \tilde{\phi}_i(x_{i,t-1}) &= \sum_{\mathbf{x}_t} Q(\mathbf{x}_t) [x_{i,t-1} h_{i,t}(\mathbf{x}_t) - \psi(h_{i,t}(\mathbf{x}_t))] \\ &\approx \int \mathcal{D}_z \gamma(g_{i,t} + z \sqrt{\Delta_{i,t}}), \end{aligned} \quad (65)$$

where $\mathcal{D}_z = \frac{dz}{\sqrt{2\pi}} \exp(-\frac{1}{2}z^2)$.

Then, the backward conditional entropy is written as

$$\begin{aligned}\sigma_t^{\text{backward}} &= - \sum_{\mathbf{x}_{t-2}} \sum_{\mathbf{x}_{t-1}} p(\mathbf{x}_{t-1}|\mathbf{x}_{t-2}) Q(\mathbf{x}_{t-2}) \tilde{\phi}(x_{i,t-1}) \\ &= - \sum_i \sum_{x_{i,t-1}} \left(\sum_{\mathbf{x}_{t-2}} p(x_{i,t-1}|\mathbf{x}_{t-2}) Q(\mathbf{x}_{t-2}) \right) \tilde{\phi}(x_{i,t-1})\end{aligned}\quad (66)$$

Note that, from Eq. 51, we have

$$\begin{aligned}m_{i,t} &= \sum_{\mathbf{x}_{t-1}} p(\mathbf{x}_t = 1|\mathbf{x}_{t-1}) p(\mathbf{x}_{t-1}) \simeq \sum_{\mathbf{x}_{t-1}} p(\mathbf{x}_t = 1|\mathbf{x}_{t-1}) Q(\mathbf{x}_{t-1}), \\ 1 - m_{i,t} &= \sum_{\mathbf{x}_{t-1}} p(\mathbf{x}_t = 0|\mathbf{x}_{t-1}) p(\mathbf{x}_{t-1}) \simeq \sum_{\mathbf{x}_{t-1}} p(\mathbf{x}_t = 0|\mathbf{x}_{t-1}) Q(\mathbf{x}_{t-1}).\end{aligned}\quad (67)$$

Applying these equations for the case of $t - 1$, we obtain

$$\begin{aligned}\sigma_t^{\text{backward}} &\simeq - \sum_i \left\{ m_{i,t-1} \tilde{\phi}(x_{i,t-1} = 1) + (1 - m_{i,t-1}) \tilde{\phi}(x_{i,t-1} = 0) \right\}, \\ &\simeq - \sum_i \left\{ m_{i,t-1} (\tilde{\phi}(x_{i,t-1} = 1) - \tilde{\phi}(x_{i,t-1} = 0)) + \tilde{\phi}(x_{i,t-1} = 0) \right\}.\end{aligned}\quad (68)$$

Thus it can be obtained by computing the two Gaussian integral terms.

Since this equation can be further computed as

$$\sigma_t^{\text{backward}} \simeq - \sum_i \left\{ m_{i,t-1} (\tilde{\phi}(x_{i,t-1} = 1) - \tilde{\phi}(x_{i,t-1} = 0)) + \tilde{\phi}(x_{i,t-1} = 0) \right\}.\quad (69)$$

and

$$\begin{aligned}\tilde{\phi}(x_{i,t-1} = 1) - \tilde{\phi}(x_{i,t-1} = 0) &= \sum_{\mathbf{x}_t} Q(\mathbf{x}_t) h_{i,t}(\mathbf{x}_t), \\ \tilde{\phi}(x_{i,t-1} = 0) &= - \sum_{\mathbf{x}_t} Q(\mathbf{x}_t) \psi(h_{i,t}(\mathbf{x}_t)),\end{aligned}\quad (70)$$

it becomes

$$\sigma_t^{\text{backward}} = - \sum_i \sum_{\mathbf{x}_t} Q(\mathbf{x}_t) [m_{i,t-1} h_{i,t}(\mathbf{x}_t) - \psi(h_{i,t}(\mathbf{x}_t))],\quad (71)$$

which is equivalent to Eq. 57 in Methods and can be also approximated by the Gaussian integral.

2 S2 text. The d-prime measure

Here, we provide the definition of the primary behavioral metric, d' (*d-prime*), for clarity. This follows the white paper of “Allen Brain Observatory: Visual Behavior Neuropixels”, where further details are available.

To evaluate the sensitivity of the mice to the stimulus, the primary behavioral metric, d' (*d-prime*), was calculated using data detected only in the active condition with visual changes. The formula for d' is as follows:

$$d' = Z(R_H) - Z(R_F), \quad (72)$$

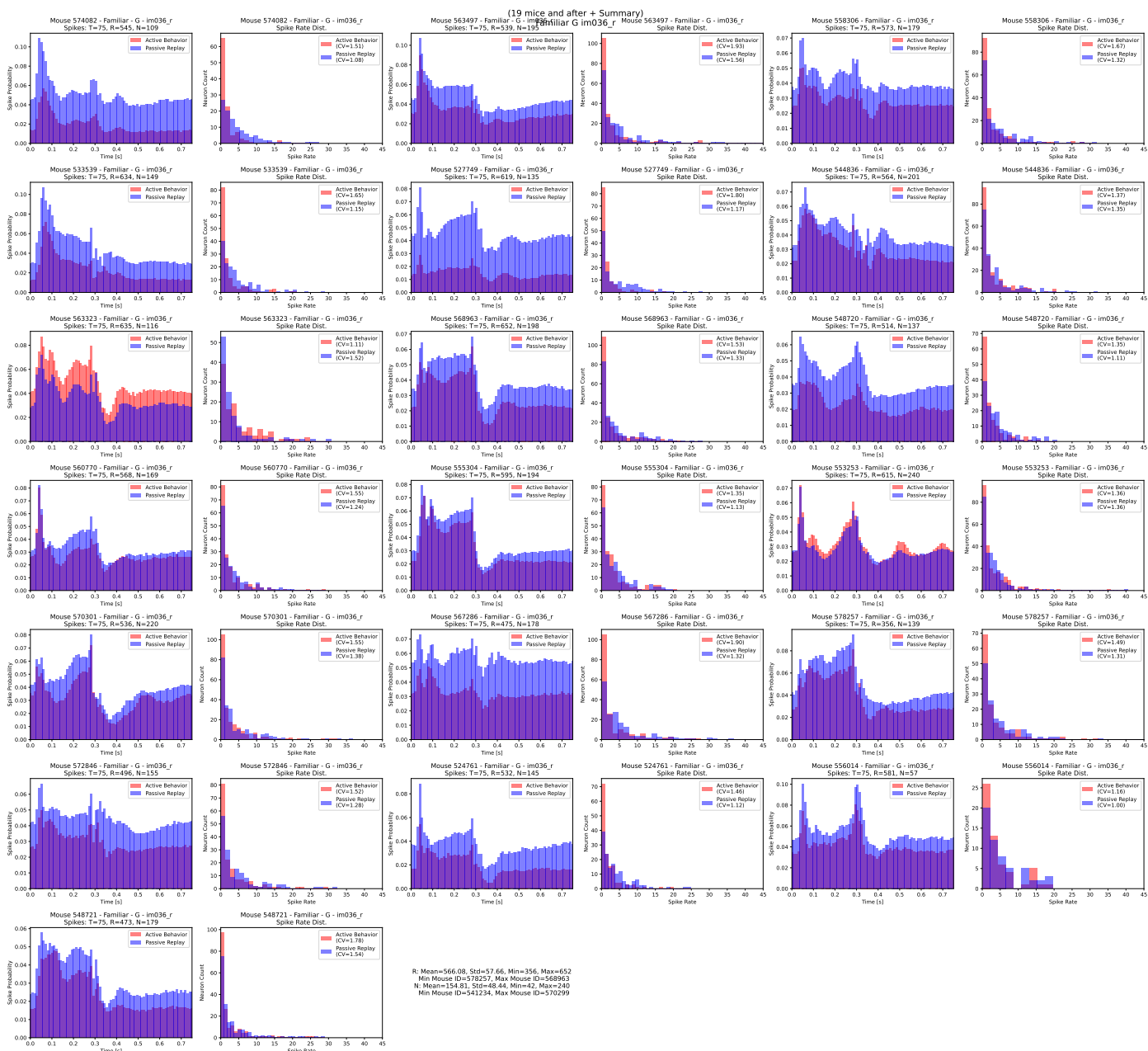
where R_H is the hit rate (the proportion of trials in which the mouse correctly responded to a change in the visual stimulus), and R_F is the false alarm rate (the proportion of trials in which the mouse incorrectly responded to a non-existent change). The function Z represents the inverse of the cumulative distribution function of a standard normal distribution, converting the hit and false alarm rates into z-scores. To prevent extreme values (e.g., 0 or 1) from distorting the results, R_H and R_F were adjusted using the following boundary equations:

$$\frac{1}{2N_H} \leq R_H \leq 1 - \frac{1}{2N_H}, \quad \frac{1}{2N_F} \leq R_F \leq 1 - \frac{1}{2N_F}, \quad (73)$$

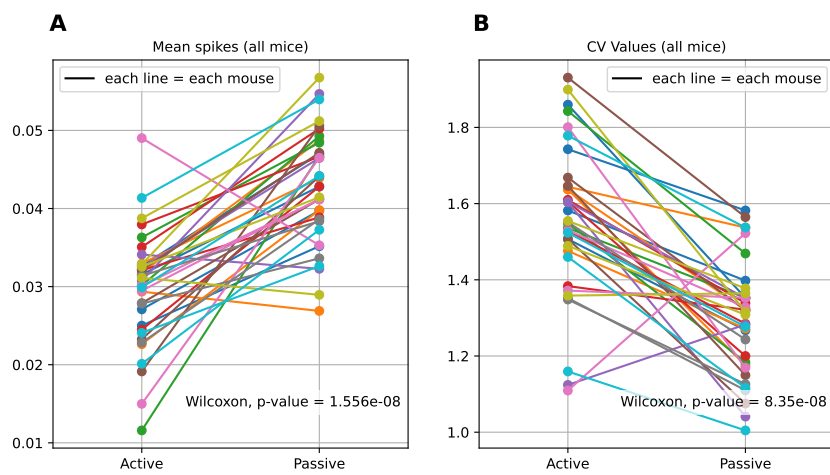
where N_H and N_F are the total number of trials for the hit and false alarm conditions, respectively. To assess the overall behavioral performance across sessions or experimental conditions, mean d' was used as an aggregated measure, representing the average d' over multiple trials or sessions. For more details, see also [73].



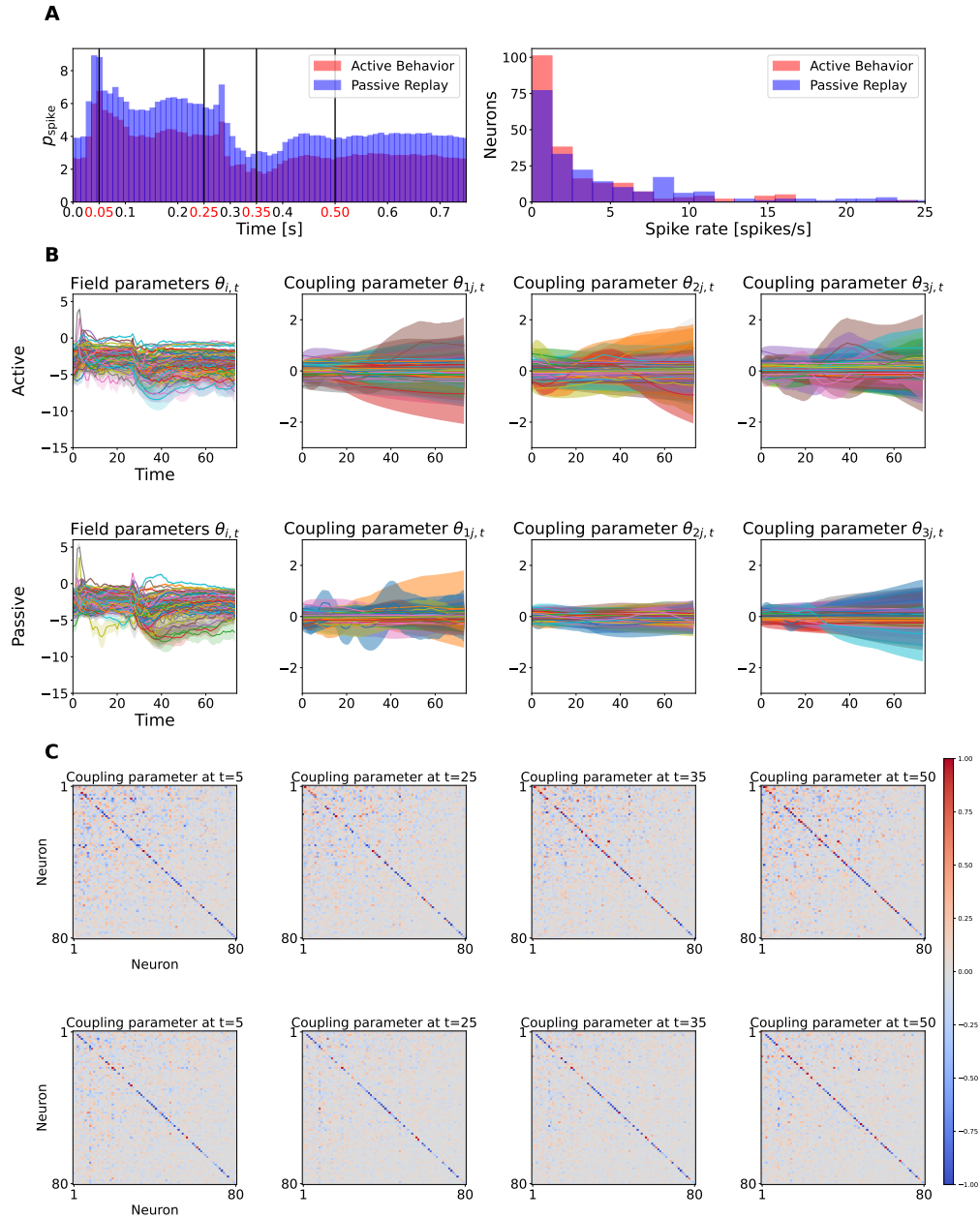
S1 Fig. Spike-rate dynamics and distributions for mice 1-18 Spike-rate dynamics and distributions under the active (red) and passive (blue) conditions. The presentation styles for each mouse follow Fig. 5A. The mice were listed in descending order of behavioral performance measured by d-prime. See Fig. S2 Fig for the remaining mice.



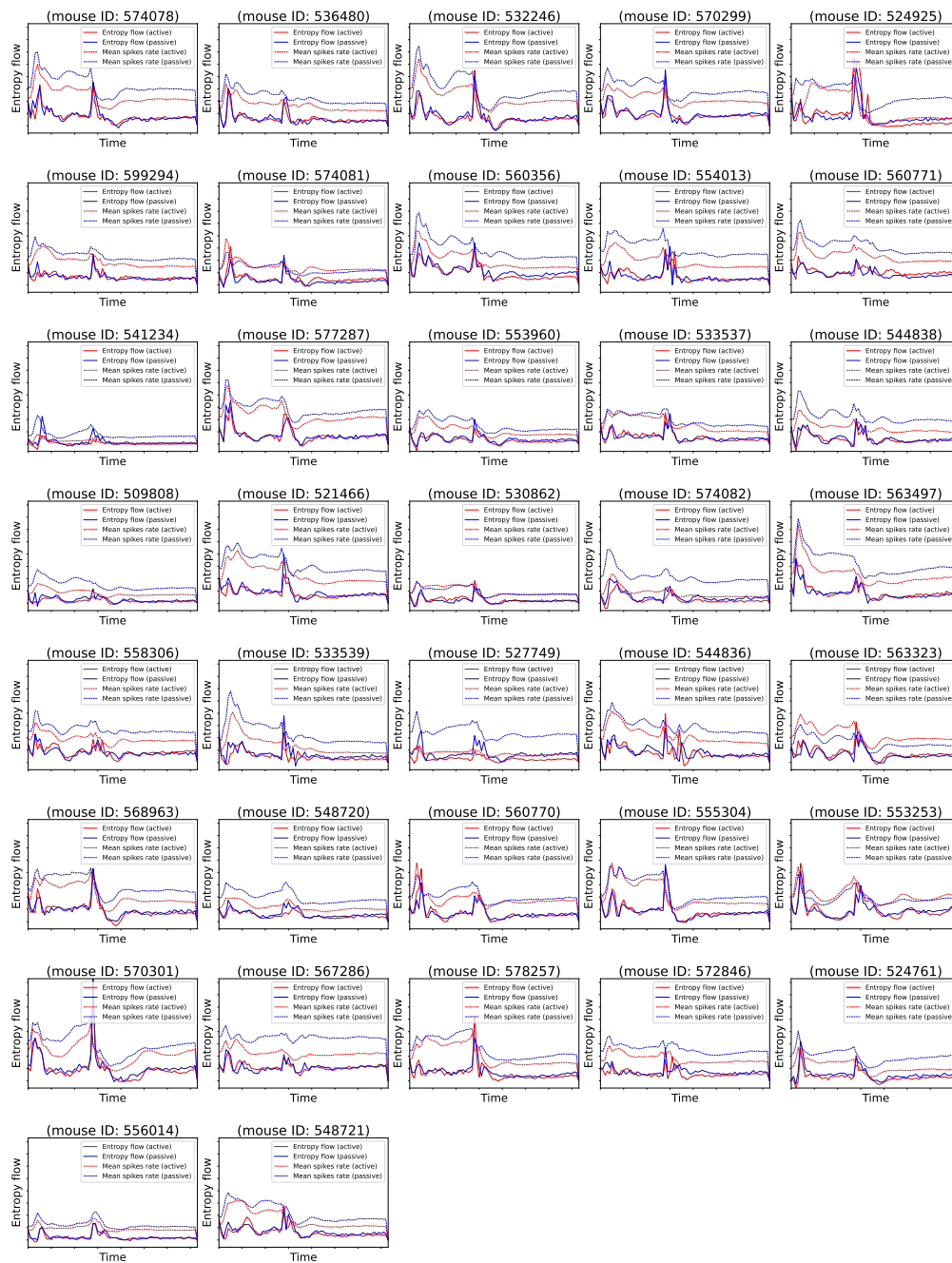
S2 Fig. Spike-rate dynamics and distributions for mice 19-37 The same as in S1 Fig but for the remaining 19 mice.



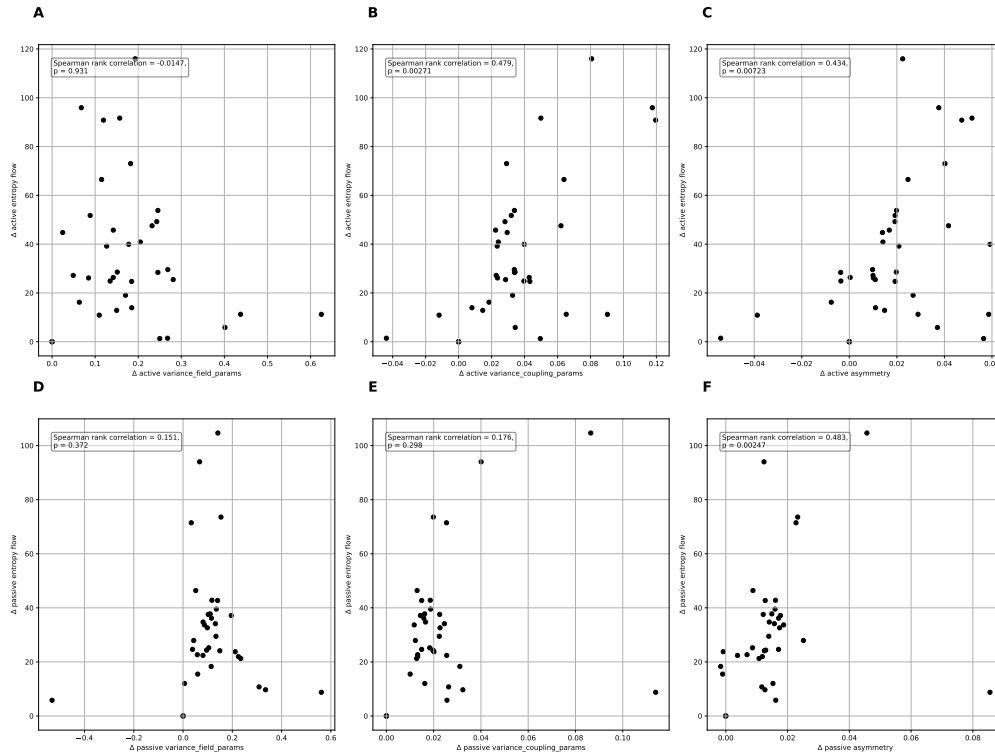
S3 Fig. Comparison of mean spike rates and coefficient of variation in the active and passive conditions. **A** Mean spiking probability across all bins, trials, and neurons in active and passive conditions. Each line represents the same mouse. Neurons showed significantly lower firing rates in the active condition ($p = 1.556 \times 10^{-8}$, Wilcoxon signed-rank test). **B** Coefficient of variations (CVs) of the firing rate distributions, a measure of sparseness, in the active and passive conditions. CV was significantly higher in the active condition ($p = 8.35 \times 10^{-8}$, Wilcoxon signed-rank test).



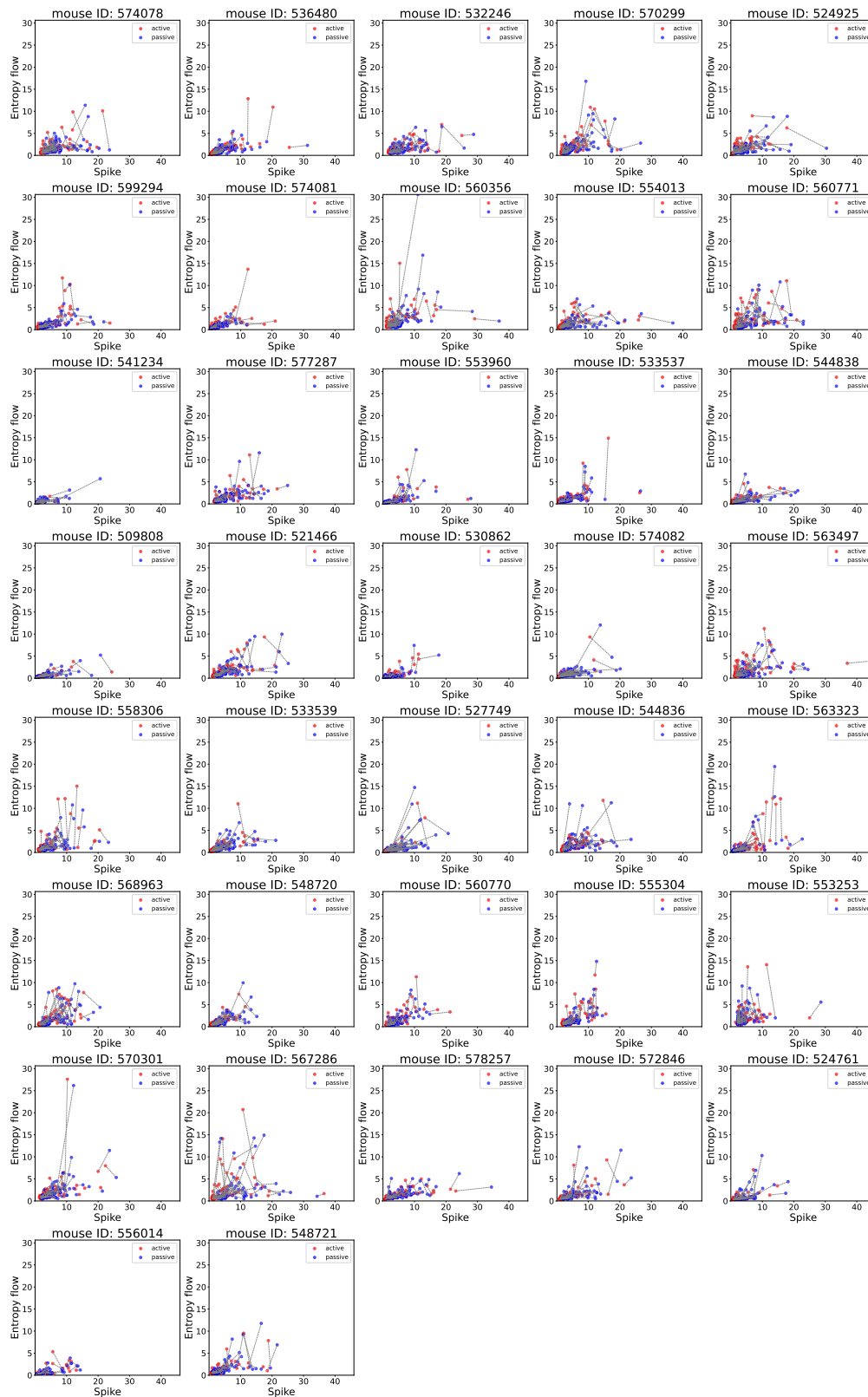
S4 Fig. Estimated neural dynamics under active and passive conditions in shuffled data of mouse 574078. Presentation style follows Fig. 5.



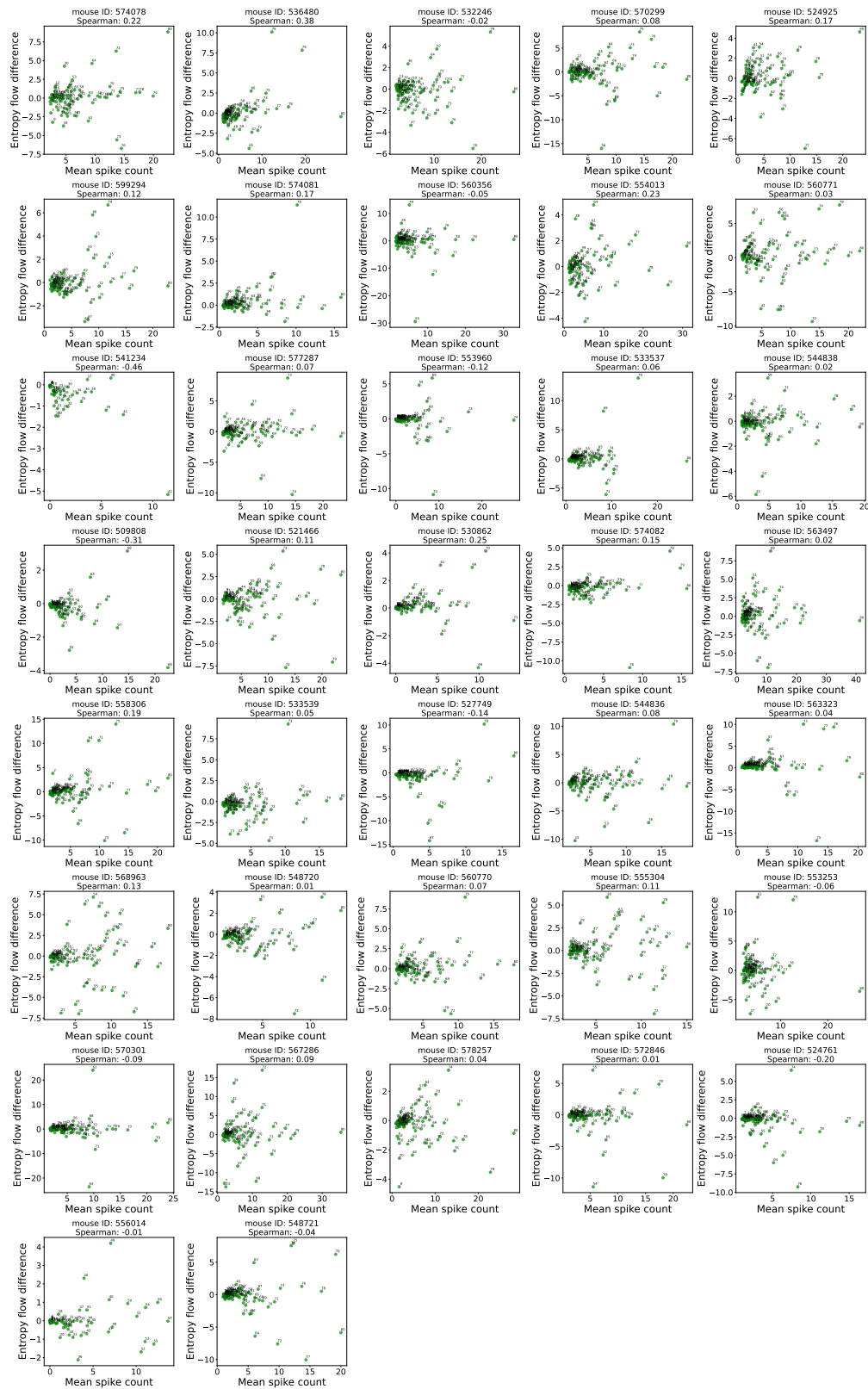
S5 Fig. Time courses of entropy flow and mean spike rates for each mouse under active and passive conditions. Each subplot represents the dynamics of an individual mouse. Solid lines are entropy flows (red for active, blue for passive) while dashed lines represent the average population spike rate (red for active, blue for passive).



S6 Fig. Comparison of significant parameter variabilities and coupling asymmetry with entropy flow for all mice. Each row represents comparisons of significant parameter variabilities and coupling asymmetry (calculated by subtracting the shuffled-data estimate of the variance from the original-data estimate) and their relationship to the shuffle-subtracted entropy flow. **A, B, C** “ Δ active” (significant changes in the field, coupling variabilities, and coupling asymmetry) versus the shuffle-subtracted entropy flow in the active state. **D, E, F** “ Δ passive” versus the shuffle-subtracted entropy flow in the passive state.



S7 Fig. Distributions of mean spike rates and entropy flows for all mice. Each point represents a unit under active (red) and passive (blue) conditions. Dashed lines connect the same units.



S8 Fig. Entropy flow difference versus mean spike counts for all mice. Each subplot represents an individual mouse. The x-axis is the geometric mean of spike counts under active and passive conditions while the y-axis is the entropy flow difference between these conditions. Each data point corresponds to one neuron with labels indicating neuron indices.